Wang, X. T., Sigman, D. M., Prokopenko, M., Adkins, J. F., Robinson, L., Hines, S. K., Chai, J., Martinez Garcia, A., Chen, T., & Haug, G. H. (2017). Deep-sea coral evidence for lower Southern Ocean surface nitrate concentrations during the last ice age. *Proceedings of the National Academy of Sciences of the United States of America*, *114*(13), 3352–3357. https://doi.org/10.1073/pnas.1615718114

Classification: PHYSICAL SCIENCES: Earth, Atmospheric, and Planetary Sciences

Title: Deep-sea coral evidence for lower Southern Ocean surface nitrate concentrations during the last ice age

Short title: Ice age nutrient consumption in the Southern Ocean

Authors: Xingchen T. Wang[a,1], Daniel M. Sigman[a], Maria G. Prokopenko[b], Jess F. Adkins[c], Laura F. Robinson[d], Sophia K. Hines[c], Junyi Chai[e], Anja S. Studer[f], Alfredo Martínez-García[f], Tianyu Chen[d], Gerald H. Haug[f,g]

Author affiliations: [a]Department of Geosciences, Princeton University, Princeton, NJ 08544; [b]Department of Geology, Pomona College, Claremont, CA 91711; [c]Division of Geology and Planetary Sciences, Caltech, Pasadena, CA 91125; [d]School of Earth Sciences, University of Bristol, Bristol, BS81RJ, UK; [e]Atmospheric and Oceanic Sciences Program, Princeton University, NJ 08544; [f]Climate Geochemistry Department, Max Planck Institute for Chemistry, Mainz 55128, Germany; [g]Geological Institute, ETH Zürich, Zürich 8092, Switzerland

[1]To whom correspondence should be addressed. Email: xingchen@princeton.edu; telephone: 609-937-2536.

Keywords: Southern Ocean, nutrient consumption, atmospheric CO_2, ice ages;

Abstract

The Southern Ocean regulates the ocean's biological sequestration of CO_2 and is widely suspected to underlie much of the ice age decline in atmospheric CO_2 concentration, but the specific changes in the region are debated. While more complete drawdown of surface nutrients by phytoplankton during the ice ages is supported by some sediment core-based measurements, the use of different proxies in different regions has precluded a unified view of Southern Ocean biogeochemical change. Here, we report measurements of the $^{15}N/^{14}N$ of fossil-bound organic matter in the stony deep-sea coral *Desmophyllum dianthus*, a new tool for reconstructing surface ocean nutrient conditions. The central robust observation is of higher $^{15}N/^{14}N$ across the Southern Ocean during the Last Glacial Maximum (LGM), 18-25,000 years ago. These data suggest a reduced summer surface nitrate concentration in both the Antarctic and Subantarctic Zones during the LGM, with little surface nitrate transport between them. After the ice age, the increase in Antarctic surface nitrate occurred through the deglaciation and continued in the Holocene. The rise in Subantarctic surface nitrate appears to have had both early deglacial and late deglacial/Holocene components, preliminarily attributed to the end of Subantarctic iron fertilization and increasing nitrate input from the Antarctic, respectively.

Significance Statement

The concentration of carbon dioxide in the atmosphere (pCO_2) varies by 80-100 ppm on glacial-interglacial timescales, with lower pCO_2 during the ice ages. In the

modern Southern Ocean, the surface nutrients are not fully consumed by phytoplankton, resulting in leakage of deeply sequestered CO_2 to the atmosphere. It has been suggested that more complete nutrient consumption in the Southern Ocean would have caused the lower pCO_2 during the ice ages. Here, we provide the most spatially comprehensive evidence to date in support of the proposal that the entire Southern Ocean was nutrient-depleted during the last ice age relative to modern conditions. These data are consistent with the hypothesis that Southern Ocean changes underlie the lower atmospheric pCO_2 of the ice ages.

\body

Introduction

Phytoplankton grow in the sunlit surface waters of the ocean, transforming carbon dioxide (CO_2) into organic carbon, and the portion of this organic carbon that sinks out of the surface ocean ("export production") effectively transfers CO_2 from the surface waters and the overlying atmosphere into the dark, deep ocean. In parallel with carbon, the nutrients required in large quantities by all phytoplankton (the "major nutrients" nitrogen, N, and phosphorus, P) are also exported out of the surface ocean and stored in the deep ocean. The "efficiency" of the biological pump is a global measure of the degree to which marine organisms exploit the major nutrients in the ocean to produce sinking organic matter. A higher efficiency of the biological pump stores more CO_2 in the deep ocean, lowering the partial pressure of CO_2 (pCO_2) in the atmosphere (1).

In today's Southern Ocean, phytoplankton consume only a small fraction of the available N and P, due to limitation by light and the trace nutrient iron (2, 3), resulting in leakage of deeply stored CO_2 through the Southern Ocean surface and back to the atmosphere and a less efficient biological pump (4). Changes in the degree of N and P consumption in the Southern Ocean may have played a role in past changes in atmospheric partial pressure of carbon dioxide (pCO_2), especially on glacial-interglacial timescales (5). Since the discovery that the ice age pCO_2 was ~1/3 lower than the pre-industrial pCO_2 (6), research has been ongoing to reconstruct the biogeochemistry of the Southern Ocean over glacial cycles (5, 7, 8). Relative to interglacials such as the Holocene, reconstructed ice age export production was higher in the Subantarctic zone (SAZ) but lower in the Antarctic zone (AZ) (5, 9). Understanding this pattern requires additional biogeochemical information. A complementary constraint, and the more central one for air-sea CO_2 exchange, is how the degree of nutrient consumption varied in each of these two zones of the Southern Ocean.

The nitrogen isotopic composition of organic matter has the potential to record the degree of nitrate consumption in Southern Ocean surface waters in the past. During nitrate uptake, phytoplankton preferentially consume ^{14}N relative to ^{15}N, resulting in a correlation between the $\delta^{15}N$ of sinking organic matter and the fraction of the nitrate supply consumed in the surface ocean, where $\delta^{15}N = [(^{15}N/^{14}N)_{sample}/ (^{15}N/^{14}N)_{air}]-1$. The early application of this correlation was with bulk sedimentary N (10). However, bulk sedimentary $\delta^{15}N$ can be biased due to diagenetic alteration and contamination by foreign N input, with evidence for major artifacts from these processes in sediment records from

both low and high latitude sites (11, 12). The $\delta^{15}N$ of organic matter bound within diatom and foraminifera microfossils avoids these issues and have been applied to reconstruct the nitrate consumption in the AZ and SAZ of the Southern Ocean, respectively (12, 13).

To complement isotopic studies of planktonic microfossil-bound N, we have pursued the nitrogen isotopic composition of organic matter bound within the carbonate skeleton of deep-sea scleractinian corals (14). Relative to the sedimentary microfossil-based $\delta^{15}N$ records, deep-sea coral have the advantages that: (1) Deep-sea corals feed on organic matter that derives from the sinking flux out of the surface ocean, benefitting from the mass balance that drives the correlation between the $\delta^{15}N$ of N export and the degree of nitrate consumption in surface waters (14); (2) deep-sea corals can be precisely dated with U-Th and radiocarbon methods, with each coral being an independent constraint on past conditions; (3) Deep-sea corals exist in both the SAZ and AZ and thus provide a complete picture of the Southern Ocean from a single fossil type, down to the species level. The >250 fossil corals used in this study are collected from the Drake Passage (DP), with collection sites in both the SAZ and AZ, and from the SAZ south of Tasmania (Fig. 1). All the corals used in this study are of the solitary species *Desmophyllum dianthus*, avoiding potential complications associated with species change over time. The corals were dated by radiocarbon, with ~50 of them also dated using uranium-thorium techniques (Fig. 2). Prior work dating these corals by both approaches provides a basis for the radiocarbon reservoir age correction (15, 16). The five coral sites in the Drake Passage can be separated into an SAZ group (Burwood Bank and Cape Horn, to the north

112 of the subantarctic front) and an AZ group (Sars, Interim and Shackleton Fracture Zone,
113 to the south of the subantarctic front, Fig. 1).

114

115 **Results and Discussion**

116 Our coral sites cover a wide range of surface nitrate concentration ($[NO_3^-]$) from >20 μM
117 in the DP AZ, to ~15 μM in the DP SAZ, to ~3 μM in the Tasmanian SAZ (Fig. 1). Our
118 late Holocene (0-5 kyr) average coral $\delta^{15}N$ in the Tasmanian SAZ (10.34 ± 0.99‰, 1σ,
119 n=37) is higher than that of the DP SAZ (8.60 ± 0.95‰, 1σ, n=26) and AZ (9.01 ±
120 1.07‰, 1σ, n=16), with the DP AZ and SAZ coral $\delta^{15}N$ indistinguishable from one
121 another. These values are consistent with expectations based on the Rayleigh model,
122 given the conditions in these regions (*SI text*).

123

124 The $\delta^{15}N$ range in corals of similar ages (Fig. 2a) is far greater than the analytical
125 uncertainty (1sd = 0.2‰; (17, 18)). Complementing this inter-specimen variability,
126 analyses from individual coral septa along the growth direction show $\delta^{15}N$ variation of 1-
127 2‰ on what would represent decadal timescales (Fig. S2). Such inter- and intra-specimen
128 $\delta^{15}N$ variation may record region-wide changes in the $\delta^{15}N$ of N export, which would be
129 of interest. Alternatively, they may be biological (e.g., ontogenetic) and/or may result
130 from short time scale changes in deep particle transport that alter the $\delta^{15}N$ of the food
131 supply to the corals. Measurements of recent corals at individual sites suggest $\delta^{15}N$
132 variation of as much as 2‰ in coral carbonate-bound N at a given oceanic site (e.g., as a
133 function of depth) (14), raising the possibility of this degree of inherent variation,

134 although decadal variation in the regional $\delta^{15}N$ of N export may also be contributing to
135 the range in recent coral $\delta^{15}N$ at the test sites. Among the Southern Ocean corals studied
136 here (Fig. S2) and others that have been investigated (14), there is no shared trend in $\delta^{15}N$
137 through individual septa. Thus, the $\delta^{15}N$ variability both within septa and across
138 specimens is best explained by environmental variability, as opposed to an ontogenetic
139 effect, but this does not allow us to distinguish between regional change in sinking N
140 $\delta^{15}N$ (the signal of interest) and local deep particle dynamics. Further ground-truthing
141 will be required to assess the significance of such short time scale variation in coral $\delta^{15}N$,
142 which we avoid interpreting here. However, it is worth noting that there may be changes
143 in inter-specimen $\delta^{15}N$ variability through the records, for example, greater variability
144 between 15 and 13 kyr; if confirmed, this may yield important insights into past
145 biogeochemical and environmental conditions. While the inherent high temporal
146 resolution of deep-sea corals raises their potential for studying high-frequency marine N
147 cycle dynamics in the past, it currently complicates the identification of modest
148 millennial scale changes. We focus here on the large-scale, long-term trends over the past
149 40 kyr, which, due to the large number of corals analyzed, emerge despite short-term
150 variability. Monte Carlo and Kalman filter methods are used that incorporate all
151 characterized uncertainties (Fig. 2, Material and Methods).

152

153 **Antarctic Zone**

154 In the Antarctic Zone of the Southern Ocean, diatom-bound $\delta^{15}N$ records generally
155 indicate more complete nitrate consumption during the last glacial period, but the records
156 vary among cores (8), with an opposite change in the Pacific and Atlantic sectors of the

AZ (19), and there are concerns of strong effects from diatom species differences (20). The average coral $\delta^{15}N$ is 4-5 ‰ higher during the LGM than the late Holocene (Fig. 2d), consistent with a recent diatom-bound $\delta^{15}N$ record from the Pacific AZ near the Antarctic Polar Front (Figs. 1, 3), where diatom species changes are minor (13). Using the Rayleigh model, we convert the $\delta^{15}N$ records to the degree of summertime nitrate consumption (the percentage of the wintertime surface nitrate that is consumed over the summer productive period; *SI text*). Both records indicate that the surface nitrate consumption was >90%. Assuming no change in the $[NO_3^-]$ or $\delta^{15}N$ of underlying Circumpolar Deep Water (which is justified by the observation that the modern values are close to the whole-ocean averages), we calculate a summertime surface $[NO_3^-]$ of <5 μM in the LGM Antarctic (*SI text* and Fig. S8). The constriction of the Drake Passage causes the AZ there to integrate conditions across most of the latitude range of the AZ in other sectors. Thus, the coral $\delta^{15}N$ data provide the strongest evidence to date that the ice age increase in nitrate consumption did not apply solely to sites near the Antarctic Polar Front but rather applied to the full latitude range of the AZ.

Subantarctic Zone

In the Tasmanian SAZ record (Fig. 2b), the average coral $\delta^{15}N$ is 4-5‰ higher during the LGM than the late Holocene, an observation consistent with a foraminifera-bound $\delta^{15}N$ record in the Atlantic SAZ (Fig. 3b) (12). The Tasmania SAZ coral $\delta^{15}N$ record is further corroborated by the coral $\delta^{15}N$ compilation from the Drake Passage SAZ. In the Drake Passage SAZ, no *D. dianthus* older than ~17 kyr were found (21). Nevertheless, coral $\delta^{15}N$ also shows a 3.5-4.0‰ decrease from ~15 kyr to the late Holocene (Fig. 2c). In sum,

180 the SAZ deep sea coral $\delta^{15}N$ data greatly strengthen the N isotopic evidence for more
181 complete nitrate consumption in the ice age SAZ. Combining these results with those
182 from the AZ, both of the major zones of the Southern Ocean were characterized by more
183 complete nitrate consumption during the last ice age.

184

185 Questions exist regarding particle dynamics in the Southern Ocean and specifically the
186 role that circulation may play in the $\delta^{15}N$ distribution of deep suspended particles, and
187 this is a concern for paleoceanographic applications of Southern Ocean deep sea corals. It
188 would seem plausible that deep sea particle could be exchanged between the AZ and
189 SAZ, leading to an erroneous interpretation from deep sea corals regarding nutrient
190 conditions in their region of growth; for example, the SAZ coral $\delta^{15}N$ might be argued to
191 respond to AZ nutrient conditions. A range of observations and considerations argue
192 against the dominance of such an effect for the last 40 kyr. First, the ~2‰ higher $\delta^{15}N$ of
193 modern corals in the Tasmanian SAZ relative to the Drake Passage (Fig. S3) is consistent
194 with local sinking particles dominating the food source to corals in each region. Given
195 the evidence for low productivity in the AZ during ice ages (9), contamination of the
196 SAZ by AZ particles would be even less likely during the LGM, and the circulation of
197 the Southern Ocean is inconsistent with SAZ particles substantially influencing the AZ.
198 Second, the Tasmanian SAZ and Drake Passage AZ coral $\delta^{15}N$ records have coherent
199 differences (Fig. 2b versus Fig. 2d) that argue against the same history of change being
200 recorded by both regions. Third, the Tasmanian corals are from the northern margin of
201 the SAZ, quite distant from the AZ (Fig. 1), such that most deep particles from the AZ
202 would be decomposed prior to reaching this far north. Fourth, the deep-sea coral $\delta^{15}N$

records are remarkably consistent with both AZ diatom $\delta^{15}N$ and SAZ foraminifera $\delta^{15}N$ (Fig. 3), and these microfossil-forming plankton are not sensitive to deep suspended particle $\delta^{15}N$. Thus, we believe that the interpretation of more complete nitrate consumption across the Southern Ocean during the last ice age is robust.

The Subantarctic Zone sits downstream of the Antarctic Zone in the large-scale overturning circulation and today receives a significant fraction of its nitrate from the AZ mixed layer. Because the surface [NO_3^-] during the LGM was much lower than today in the AZ, the contribution of the AZ surface to nitrate in the SAZ thermocline and surface mixed layer was lower during the LGM. We simulate this effect with a mixing model (Fig. S7, *SI text*), using the reconstructed changes in AZ [NO_3^-] over the last 40 kyr (Fig. S8a). The mixing model also indicates that the $\delta^{15}N$ of the gross nitrate supply to the SAZ would have varied in response to changes in AZ nitrate concentration and $\delta^{15}N$ (Fig. S7). The $\delta^{15}N$ of the nitrate supply to the SAZ is calculated to have been similar during the LGM and in the late Holocene, but with a deglacial maximum (~1.5‰ higher than the LGM and late Holocene values) (Fig. S6). The estimated rate and $\delta^{15}N$ of nitrate supply to the SAZ are combined with the reconstructed degree of nitrate consumption for the SAZ to yield a preliminary calculation of the history of [NO_3^-] in the SAZ summer mixed layer (Fig. S8b). As with the AZ, during the LGM, the SAZ surface [NO_3^-] was <5 μM (Fig. S8b). We caution that our quantitative reconstruction of ice age surface [NO_3^-] has uncertainties that are poorly characterized. In particular, the SAZ reconstruction relies on changes in nitrate supply that derive from the mixing model, in which the water exchange terms are poorly known today and could also have changed as a function of climate.

Numerical modeling frameworks calibrated with modern data have great potential to improve the reconstructions.

To explain lower ice age pCO_2, a higher degree of nitrate consumption during ice ages has been proposed for both the AZ and the SAZ (4, 22-24). Our coral $\delta^{15}N$ data provide evidence in support of these hypotheses. Remarkably, while the degree of nitrate consumption was higher in both of these regions during the last ice age, the AZ is reconstructed to have hosted much slower biological productivity than during the Holocene while the SAZ apparently hosted higher productivity (Fig. 4, (5, 9)). This has led to the interpretation of a circulation-driven ice age reduction in nitrate supply as the ultimate driver of the AZ nitrate consumption change (13), while ice age iron fertilization best explains the nitrate consumption increase in the SAZ (Fig. 4d) (12). Given these different mechanisms for changes in surface nitrate, one would not expect identical histories for nitrate consumption in the two regions. Indeed, there are distinctions in the coral $\delta^{15}N$ records from the AZ and SAZ both within the last ice age and since the end of the ice age. Below, we focus on the latter.

Deglacial changes across the Southern Ocean

Combined with the foraminifera and diatom $\delta^{15}N$ records (12, 13), our coral $\delta^{15}N$ data allow us to compare the deglacial changes in the Southern Ocean $[NO_3^-]$ with other relevant environmental changes (Fig. 4). In the AZ, $[NO_3^-]$ rose from the LGM to ~12 kyr, suggesting that the AZ contributed to the deglacial rise in atmospheric pCO_2. Export

production in the AZ rose during the same period, consistent with the previous suggestion of a deglacial rise in Southern Ocean overturning (10, 13). Interestingly, $[NO_3^-]$ in the AZ continued to increase throughout the Holocene. This feature suggests a rise in the Southern Ocean overturning in the Holocene that may have contributed to the rise in atmospheric pCO_2 since 8 kyr (25).

In the SAZ, both the coral and foraminifera $\delta^{15}N$ records suggest that there were two episodes of deglacial rise in surface $[NO_3^-]$ (Figs. 3, 4). Decreasing iron flux can explain the early to mid-deglacial increase in $[NO_3^-]$, consistent with ice age iron fertilization in the SAZ (12, 23). However, the second episode of increase in $[NO_3^-]$ during the later deglaciation and early Holocene cannot be explained solely by a change in the iron flux, which was low and relatively stable during this period (Fig. 4d). In the iron-limited SAZ, nitrate consumption is modulated by the ratio of rates of iron and nitrate supply. Without significant change in the atmospheric iron flux during the late deglaciation and early Holocene, the second episode of deglacial rise in the SAZ $[NO_3^-]$ is consistent with an increasing supply of nitrate from the AZ into the SAZ, an expected consequence of the reconstructed rise in AZ surface $[NO_3^-]$. A complication for the deglaciation is that frontal migration likely also changed the $[NO_3^-]$ field, shifting lower $[NO_3^-]$ poleward. This may have countered the deglacial rise in Southern Ocean surface $[NO_3^-]$, contributing to its apparently gradual nature.

Conclusion

From this first application of deep-sea coral $\delta^{15}N$, we reconstruct an ice age Southern Ocean without the high [NO_3^-] or the strong north-south [NO_3^-] gradient that characterize the region today. The picture that arises is of an ice age Southern Ocean state radically different from the modern, in which the two major zones (the Antarctic and the Subantarctic) receive most of their nitrate from below and consume almost all of it in the summertime surface mixed layer. This argues strongly for a central role of the biogeochemistry of the Southern Ocean in lowering ice age pCO_2.

At the same time, the data appear to indicate that the Southern Ocean [NO_3^-] rise of the last deglaciation was incomplete, with additional change through the Holocene (Fig. 4b). Given model calculations of the pCO_2 decline achieved by different Southern Ocean changes (22), the incomplete nature of Southern Ocean biogeochemical change across the early deglaciation suggests that it was not the sole driver of the early deglacial pCO_2 rise. The warming-driven decline in the solubility of CO_2 in the deep ocean, which appears to have occurred early in the deglaciation (26), may thus have been critical in the first deglacial increase in atmospheric pCO_2. There is as yet no evidence for such a lag of Southern Ocean biogeochemical change relative to Southern Ocean climate for prior glacial terminations (12, 13), but addressing this question requires better age constraints, such as might arise from uranium-thorium dating of deep-sea corals from those terminations.

Materials and Methods

Deep-sea coral collection

Deep-sea fossil corals in the Drake Passage were collected by dredge or trawl (21) while a deep submergence vehicle was used to collect coral samples from the Tasmanian seamounts (27). Detailed information on all coral samples used in this study is given in (15, 16).

Radiocarbon dating

From each individual coral, a small piece (~40 mg) was cut and physically cleaned using a Dremel tool to remove the Fe-Mn crust. Methanol was then used to clean the samples. After these steps, the samples were radiocarbon dated with methods detailed in (28, 29). The calendar age was calculated from the measured radiocarbon content and an estimated reservoir age (15, 16, 21, 27).

Uranium-Thorium dating

A subset of the corals used in this study (~20%; shown as squares in Fig. 2) was also subjected to the uranium-thorium (U-Th) dating method (15, 16). Briefly, a piece (0.3-1g) of coral was cut and physically cleaned using a Dremel tool and then chemically cleaned following (30). After cleaning, the coral was dissolved in nitric acid to dissolve the sample and a mixed ^{236}U-^{229}Th spike added. The U and Th were separated, purified, and measured separately by multi-collector inductively coupled plasma mass spectrometer (MC-ICP-MS). All U-Th ages used in this study have been published in (15, 16).

Age model

The final age model for the three coral $\delta^{15}N$ records is composed of two parts (Fig. 2). Whenever the U-Th ages are available, they are used in the final age model as the calendar age. When U-Th ages are not available, the calendar age is calculated from the radiocarbon age after correction for the water mass radiocarbon content (i.e. reservoir effect), based on the reservoir ages of coral samples for which both U-Th ages and radiocarbon ages have been measured (15, 16).

Nitrogen isotope analysis

The protocol for nitrogen isotope analysis was detailed in (14, 31, 32). Briefly, 5-10 mg of mechanically cleaned coral septum is ground into coarse powder (with a grain size of a few hundred micrometers) and sonicated for 5 minutes in 2% sodium polyphosphate in a 15 ml polypropylene centrifuge tube to remove any detrital material attached to the sample. The sample is rinsed (by filling, centrifugation, and decanting) three times with deionized water (DIW) and reductively cleaned using sodium bicarbonate buffered dithionite-citrate reagent to remove any metal coatings. After 3-4 rinses with DIW, the sample is cleaned for 24 hours using 10-15% sodium hypochlorite to remove external organic N contamination and again rinsed 3-4 times with DIW. After cleaning, the sample is dried in an oven at 60 ^{o}C and dissolved in 4 N hydrochloric acid. The released organic matter is oxidized to nitrate using a basic potassium persulfate solution. The resulting dissolved nitrate is converted bacterially into nitrous oxide, which is measured for its $\delta^{15}N$ by automated extraction and gas chromatography-isotope ratio mass

spectrometry (33). Amino acid standards with known $\delta^{15}N$ (USGS 40 and 41) are included in each batch of samples to correct for the blank associated with persulfate reagent, which is less than 2% of the total N content in an oxidized sample. Each ground sample was processed in duplicate through the entire cleaning and analysis protocol. An in-house coral standard was used in each batch of analysis as quality control and yields a long-term precision better than 0.2‰ (1σ) (31).

To evaluate the $\delta^{15}N$ variation in single septa, multiple samples were cut out along the growth direction of each single septum and analyzed for $\delta^{15}N$ using the above method. The results for these samples are shown in Fig. S2 and discussed in the main text.

Mann-Whitney U test

To evaluate the statistical significance of the coral $\delta^{15}N$ datasets, Mann-Whitney U test were performed on the $\delta^{15}N$ time series for each 5 kyr bins (except for 20-40 kyr; Fig. S3).

N isotopes *vs.* N content in corals

To evaluate the effect of N content in driving the observed trend in our coral $\delta^{15}N$, we performed a correlation analysis and showed that the coral $\delta^{15}N$ variation cannot be explained by the changes in N content in any of the three records (Fig. S4)

Monte Carlo and Kalman Filter simulation

Monte Carlo simulation and Kalman smoother were combined to obtain a best estimate

of the average $\delta^{15}N$ time series on a regular time grid and its corresponding confidence interval. First, M synthetic time series of $\delta^{15}N$ were generated by adding errors to both age and $\delta^{15}N$ measurements. The errors are normally distributed random numbers with zero mean and specified standard deviations (sd). The standard deviations for the measured age were assigned to be 500 years (typically larger than the actual measured age uncertainty), and the standard deviations for the measured $\delta^{15}N$ are from the actual measurement errors (including both analytical error and variations on single coral septa). Then, for each one of the M synthetic time series of $\delta^{15}N$, a Kalman smoother was applied to obtain the best estimate for $\delta^{15}N$ and its standard deviation on a regular time grid. For each of the best estimates, N time series were generated to represent the probability distribution of this best estimate (by adding normally distributed random numbers with zero mean and standard deviations to the time series). Thus, outcome was M x N $\delta^{15}N$ series on a regular grid. At each time, the best estimate for $\delta^{15}N$ was obtained from the average of the M x N $\delta^{15}N$ series, and the confidence interval was obtained from the sd of the M x N $\delta^{15}N$ series (plotted as 95% confidence interval (2 sd) in Fig. 2).

Acknowledgements

This work is supported by NSF grant OCE-1234664 to M.G.P. and D.M.S., the Charlotte Elizabeth Procter Fellowship of the Graduate School at Princeton University to X.T.W., and the Grand Challenges Program of Princeton University to D.M.S. We thank two anonymous reviewers for their constructive comments.

References

1. Sarmiento JL, Toggweiler JR (1984) A new model for the role of the oceans in determining atmospheric pCO_2. *Nature* 308:621–624.

2. Martin JH, Gordon RM, Fitzwater SE (1990) Iron in Antarctic waters. *Nature* 345(6271):156–158.

3. Mitchell BG, Brody EA, Holm-Hansen O, McClain C, Bishop J (1991) Light Limitation of Phytoplankton Biomass and Macronutrient Utilization in the Southern Ocean. *Limnol Oceanogr* 36(8):1662–1677.

4. Sigman DM, Hain MP, Haug GH (2010) The polar ocean and glacial cycles in atmospheric CO2 concentration. *Nature* 466(7302):47–55.

5. Kohfeld KE, Le Quere C, Harrison SP, Anderson RF (2005) Role of marine biology in glacial-interglacial CO2 cycles. *Science* 308(5718):74–78.

6. Neftel A, Oeschger H, Schwander J, Stauffer B, Zumbrunn R (1982) Ice core sample measurements give atmospheric CO2 content during the past 40,000 yr. *Nature* 295:220–223.

7. Ziegler M, Diz P, Hall IR, Zahn R (2013) Millennial-scale changes in atmospheric CO2 levels linked to the Southern Ocean carbon isotope gradient and dust flux. *Nat Geosci* 6(6):457–461.

8. Robinson RS, Sigman DM (2008) Nitrogen isotopic evidence for a poleward decrease in surface nitrate within the ice age Antarctic. *Quat Sci Rev* 27(9-10):1076–1090.

9. Jaccard SL, et al. (2013) Two Modes of Change in Southern Ocean Productivity Over the Past Million Years. *Science* 339(6126):1419–1423.

10. Francois R, et al. (1997) Contribution of Southern Ocean surface-water stratification to low atmospheric CO2 concentrations during the last glacial period. *Nature* 389(6654):929–935.

11. Straub M, et al. (2013) Changes in North Atlantic nitrogen fixation controlled by ocean circulation. *Nature* 501(7466):200–203.

12. Martinez-Garcia A, et al. (2014) Iron Fertilization of the Subantarctic Ocean During the Last Ice Age. *Science* 343(6177):1347–1350.

13. Studer AS, et al. (2015) Antarctic Zone nutrient conditions during the last two glacial cycles. *Paleoceanography* 30:845–862.

14. Wang XT, et al. (2014) Isotopic composition of carbonate-bound organic nitrogen in deep-sea scleractinian corals: A new window into past biogeochemical change.

Earth Planet Sci Lett 400(C):243–250.

15. Burke A, Robinson LF (2012) The Southern Ocean's role in carbon exchange during the last deglaciation. *Science* 335(6068):557–561.

16. Hines SKV, Southon JR, Adkins JF (2015) A high-resolution record of Southern Ocean intermediate water radiocarbon over the past 30,000 years. *Earth Planet Sci Lett* 432:46–58.

17. Smart SM, et al. (2015) Isotopic evidence for nitrification in the Antarctic winter mixed layer. *Global Biogeochem Cycles* 29(4):427–445.

18. DiFiore PJ, et al. (2006) Nitrogen isotope constraints on subantarctic biogeochemistry. *J Geophys Res Oceans* 111:C08016.

19. Robinson RS, Brzezinski MA, Beucher CP, Horn MGS, Bedsole P (2014) The changing roles of iron and vertical mixing in regulating nitrogen and silicon cycling in the Southern Ocean over the last glacial cycle. *Paleoceanography* 29:1179–1195.

20. Studer AS, Ellis KK, Oleynik S, Sigman DM, Haug GH (2013) Size-specific opal-bound nitrogen isotope measurements in North Pacific sediments. *Geochim Cosmochim Acta* 120:179–194.

21. Margolin AR, et al. (2014) Temporal and spatial distributions of cold-water corals in the Drake Passage: Insights from the last 35,000 years. *Deep Sea Res Part II Top Stud Oceanogr* 99:237–248.

22. Hain MP, Sigman DM, Haug GH (2010) Carbon dioxide effects of Antarctic stratification, North Atlantic Intermediate Water formation, and subantarctic nutrient drawdown during the last ice age: Diagnosis and synthesis in a geochemical box model. *Global Biogeochem Cycles* 24:GB4023.

23. Martin JH (1990) Glacial-interglacial CO_2 change: The Iron Hypothesis. *Paleoceanography* 5(1):1–13.

24. Broecker WS (1982) Glacial to interglacial changes in ocean chemistry. *Prog Oceanogr* 11(2):151–197.

25. Moreno PI, Francois JP, Moy CM, Villa-Martínez R (2010) Covariability of the Southern Westerlies and atmospheric CO2 during the Holocene. *Geology* 38(8):727–730.

26. Stott L, Timmermann A, Thunell R (2007) Southern Hemisphere and Deep-Sea Warming Led Deglacial Atmospheric CO_2 Rise and Tropical Warming. *Science* 318(5849):435–438.

27. Thiagarajan N, et al. (2013) Movement of deep-sea coral populations on climatic

timescales. *Paleoceanography* 28(2):227–236.

28. Burke A, et al. (2010) Reconnaissance dating: A new radiocarbon method applied to assessing the temporal distribution of Southern Ocean deep-sea corals. *Deep Sea Res Part I Oceanogr Res Pap* 57(11):1510–1520.

29. Bush SL, et al. (2013) Simple, rapid, and cost effective: a screening method for 14C analysis of small carbonate samples. *Radiocarbon* 55(3–4). doi:http://dx.doi.org/10.1017/S0033822200057787.

30. Cheng H, Adkins J, Edwards RL, Boyle EA (2000) U-Th dating of deep-sea corals. *Geochim Cosmochim Acta* 64(14):2401–2416.

31. Wang XT, et al. (2015) Isotopic composition of skeleton-bound organic nitrogen in reef-building symbiotic corals: A new method and proxy evaluation at Bermuda. *Geochim Cosmochim Acta* 148(C):179–190.

32. Ren H, et al. (2009) Foraminiferal Isotope Evidence of Reduced Nitrogen Fixation in the Ice Age Atlantic Ocean. *Science* 323(5911):244–248.

33. Sigman DM, et al. (2001) A bacterial method for the nitrogen isotopic analysis of nitrate in seawater and freshwater. *Anal Chem* 73(17):4145–4153.

34. Ahn J, Brook EJ (2014) Siple Dome ice reveals two modes of millennial CO2 change during the last ice age. *Nat Commun* 5:3723.

35. Lüthi D, et al. (2008) High-resolution carbon dioxide concentration record 650,000-800,000 years before present. *Nature* 453(7193):379–382.

36. Altabet MA, Francois R (1994) Sedimentary Nitrogen Isotopic Ratio as a Recorder for Surface Ocean Nitrate Utilization. *Global Biogeochem Cycles* 8(1):103–116.

37. Altabet MA, Francois R (2001) Nitrogen isotope biogeochemistry of the Antarctic Polar Frontal Zone at 170°W. *Deep Sea Res Part II Top Stud Oceanogr* 48(19-20):4247–4273.

38. Lourey MJ, Trull TW (2001) Seasonal nutrient depletion and carbon export in the Subantarctic and Polar Frontal Zones of the Southern Ocean south of Australia. *J Geophys Res Oceans* 106(C12):31463–31487.

39. Rafter PA, DiFiore PJ, Sigman DM (2013) Coupled nitrate nitrogen and oxygen isotopes and organic matter remineralization in the Southern and Pacific Oceans. *J Geophys Res Oceans* 118(10):4781–4794.

40. Deutsch C, Sigman DM, Thunell RC, Meckler AN, Haug GH (2004) Isotopic constraints on glacial/interglacial changes in the oceanic nitrogen budget. *Global Biogeochem Cycles* 18:GB4012.

41. Galbraith ED, et al. (2013) The acceleration of oceanic denitrification during deglacial warming. *Nat Geosci* 6(7):579–584.

42. Haug GH, et al. (1998) Glacial/interglacial variations in production and nitrogen fixation in the Cariaco Basin during the last 580 kyr. *Paleoceanography* 13(5):427–432.

43. Tyrrell T (1999) The relative influences of nitrogen and phosphorus on oceanic primary production. *Nature* 400(6744):525–531.

44. DiFiore PJ, et al. (2010) Poleward decrease in the isotope effect of nitrate assimilation across the Southern Ocean. *Geophys Res Lett* 37:L17601.

45. Granger J, Sigman DM, Rohde MM, Maldonado MT, Tortell PD (2010) N and O isotope effects during nitrate assimilation by unicellular prokaryotic and eukaryotic plankton cultures. *Geochim Cosmochim Acta* 74(3):1030–1040.

46. Sigman DM, Altabet MA, McCorkle DC, Francois R, Fischer G (2000) The d15N of nitrate in the Southern Ocean: Nitrogen cycling and circulation in the ocean interior. *J Geophys Res Oceans* 105(C8):19599–19614.

47. Palter JB, Sarmiento JL, Gnanadesikan A, Simeon J, Slater RD (2010) Fueling export production: nutrient return pathways from the deep ocean and their dependence on the Meridional Overturning Circulation. *Biogeosciences* 7(11):3549–3568.

Figure legends

Fig. 1. Deep-sea coral sites relative to surface nitrate concentration, ocean Fronts, and bathymetry. (a) Southern hemisphere map showing climatological austral summer (December, January and February) surface nitrate concentration (color contours), fossil coral sites (white-filled, black-rimmed circles) and ocean fronts (white dotted lines, from north to south: Subtropical Front (STF); Subantarctic Front (SAF); Polar Front (PF) and Southern Antarctic Circumpolar Current Front (SACCF)). Shown as triangles are the locations of two published sediment-based fossil $\delta^{15}N$ records (foraminifera-bound $\delta^{15}N$ at ODP Site 1090 (12) and diatom-bound $\delta^{15}N$ at PS75/072-4 (13)). (b) Bathymetric map

(color contours) centered on Tasmania showing the deep-sea coral sites (overlapping black circles), austral summer surface nitrate concentration (white contours, unit: μM) and ocean fronts (yellow lines). (c) Bathymetric map centered on Drake Passage showing the deep-sea coral sites (BB: Burwood Bank; CH: Cape Horn; SA: Sars; IN: Interim; SFZ: Shackleton Fracture Zone or SFZ), and the parameters also in (b).

Fig. 2. Nitrogen isotopes of Southern Ocean deep-sea corals. (a) All Southern Ocean corals in this study, with the error bars representing analytical precision (1σ) calculated from 2-3 replicates of the same sample; and (b-d) Southern Ocean corals grouped into the Tasmanian SAZ (b) and the Drake Passage SAZ (c) and AZ (d). In panel b-d, squares indicate corals with U-Th ages while circles denote corals with radiocarbon ages corrected for the reservoir effect. The mean $\delta^{15}N$ histories (bold lines) with error envelopes (2σ; 95% confidence interval) are simulated with Monte Carlo and Kalman Filter methods (*Material and Methods*).

Fig. 3. Comparison of coral $\delta^{15}N$ records with the sedimentary microfossil $\delta^{15}N$ records, with the $\delta^{15}N$ anomaly calculated by subtracting the modern or core-top $\delta^{15}N$ values from each record. (a) Comparison of the Drake Passage AZ coral $\delta^{15}N$ mean record with the PS75/072-4 AZ diatom $\delta^{15}N$ record (13) and (b) comparison of the SAZ coral $\delta^{15}N$ records with the ODP Site 1090 SAZ foraminifera $\delta^{15}N$ record (12).

Fig. 4. Comparison of Southern Ocean biogeochemical changes and atmospheric CO_2 concentration over the past 40 kyr. (a) atmospheric CO_2 (34, 35); (b) Average AZ and

538 SAZ $\delta^{15}N$ anomalies from coral, diatom and foraminifera records in Fig. 3; (c) SAZ and

539 AZ export productivity (12, 13); and (d) Southern Ocean dust flux as recorded in the

540 Atlantic SAZ (12)

Supporting Information

SI Text

Calculations of the summertime surface nitrate concentration in the Southern Ocean

1. Rayleigh Model

When phytoplankton consume nitrate, they preferentially remove ^{14}N relative to ^{15}N, leaving the residual nitrate pool enriched in ^{15}N and yielding a relationship between the $\delta^{15}N$ of the accumulated biomass (integrated product) and the degree of nitrate consumption/nitrate utilization (36). Thus, in ocean regions where surface nitrate is not completely consumed and there is a strong temporal separation of nitrate supply and nitrate consumption, such as the Southern Ocean (37, 38), the $\delta^{15}N$ of the accumulated biomass is an approximate proxy for the degree of nitrate consumption (Rayleigh model). Over the course of a year, the N export/sinking flux should equal the consumed nitrate, so that the $\delta^{15}N$ of the sinking flux can be described by the Rayleigh model's approximate integrated product equation:

$$(1)\ \delta^{15}N_{integrated} = \delta^{15}N_{initial} + \epsilon \times \frac{f \times \ln f}{1 - f}$$

where $\delta^{15}N_{initial}$ is the nitrate $\delta^{15}N$ prior to nitrate consumption; ϵ is the isotope effect of nitrate consumption (positive value means the product is depleted in ^{15}N relative to the substrate); and f is the fraction of remaining nitrate.

The residual nitrate $\delta^{15}N$ is approximated by:

$$(2)\ \delta^{15}N_{[NO_3^-]} = \delta^{15}N_{initial} - \epsilon \times \ln f$$

Deep-sea corals feed on organic matter that derives from this sinking flux, and the $\delta^{15}N$ of deep-sea corals has been shown to be a good proxy for the $\delta^{15}N$ of the sinking flux in the modern ocean (14).

Below we use the Rayleigh model to calculate the surface nitrate concentration in the Southern Ocean over the past 40 kyr, using our three new coral $\delta^{15}N$ datasets and the published foraminifera and diatom $\delta^{15}N$ datasets in main text Fig. 3 (12, 13). Because diatoms, foraminifera and corals are three distinct groups of organisms at different trophic levels, we normalize each $\delta^{15}N$ dataset to their modern values by simply subtracting the modern $\delta^{15}N$ values from each record, yielding the $\delta^{15}N$ anomaly (Fig. 3). We then apply the Rayleigh model to each dataset and compute the surface nitrate concentration for each of the five datasets, binning them into AZ and SAZ groups.

2. Antarctic zone summertime surface nitrate concentration since 40 kyr

In the AZ, both the coral and diatom records show on average 4-5‰ higher $\delta^{15}N$ during the LGM than the late Holocene (Fig. 3a). Applying the Rayleigh model to the AZ surface ocean:

(3) $$\delta^{15}N_{AZ-integrated} = \delta^{15}N_{UCDW} + \epsilon_{AZ} \times \frac{f_{AZ} \times \ln f_{AZ}}{1 - f_{AZ}}$$

(4) $$[NO_3^-]_{AZ} = [NO_3^-]_{UCDW} \times f_{AZ}$$

(5) $$\delta^{15}N_{[NO_3^-]AZ} = \delta^{15}N_{UCDW} - \epsilon_{AZ} \times \ln f_{AZ}$$

where Upper Circumpolar Deep Water (UCDW) is used as the starting nitrate pool ($[NO_3^-]_{UCDW}$ = 33 μM; $\delta^{15}N_{UCDW}$ = 5‰; (39)); ϵ_{AZ} is the isotope effect of nitrate consumption in the AZ surface ocean; f_{AZ} is the fraction of remaining nitrate (with a modern value of 0.7); $[NO_3^-]_{AZ}$ is the residual nitrate concentration in the AZ surface; and $\delta^{15}N_{[NO_3^-]AZ}$ is the residual nitrate δ^{15}N in the AZ surface.

As indicated in Equation (3), $\delta^{15}N_{AZ-integrated}$ is a function of three variables: $\delta^{15}N_{UCDW}$, $\epsilon_{AZ}$and f_{AZ}. It is thus important to consider the changes in the other two variables before we attribute the 4-5‰ higher LGM $\delta^{15}N_{AZ-integrated}$ to a change in the surface nitrate concentration.

For the AZ, the only source of nitrate to the winter mixed layer (which sets the initial nitrate concentration and δ^{15}N of the summer mixed layer) is mixing with and upwelling of UCDW. Thus, to change $\delta^{15}N_{initial}$ in the AZ, one has to change the UCDW nitrate δ^{15}N. One possible way to do this is to change the mean ocean nitrate δ^{15}N. However, while there is a paucity of direct evidence as to mean ocean nitrate δ^{15}N over glacial-interglacial cycles, the existing data suggest that mean ocean nitrate δ^{15}N changed very little over the past 40 kyr (40, 41). Given the evidence for N fixation feedbacks (11, 32, 42), the ocean nitrate reservoir has likely been tied to that of phosphate (43), and UCDW nitrate concentration is today similar to the mean deep ocean value. Thus, major changes in UCDW nitrate concentration are also unlikely. In all the calculations below, we assume that the nitrate concentration and δ^{15}N in UCDW have remained constant over the past 40 kyr.

A change in ϵ_{AZ} during the LGM is also possible, given the previous finding that ϵ_{AZ} varies as a function of mixed layer depth in the Southern Ocean (44). We can explore the possible contribution of changing ϵ_{AZ} to the 4-5‰ higher LGM $\delta^{15}N_{AZ-integrated}$. With given values of $\delta^{15}N_{UCDW}$, contour plot of $\delta^{15}N_{AZ-integrated}$ as a function of ϵ_{AZ} and f_{AZ} can be generated using Equation (3) (Fig. S5). It is shown that, within the range of observed isotope effect of nitrate assimilation in the modern ocean (44), the $\delta^{15}N_{AZ-integrated}$ is more sensitive to changes in f_{AZ} than in ϵ_{AZ}; especially when the surface nitrate consumption is high. The modern AZ has an average f_{AZ} value of ~0.7 and a ϵ_{AZ} value of ~6‰ (44). Since ϵ_{AZ} during the spring-to-fall nitrate drawdown is unlikely to be lower than 4‰ (45), the maximum increase in LGM $\delta^{15}N_{AZ-integrated}$ caused by a lower ϵ_{AZ} is less than 2‰ and most likely less than 1‰. When converting the δ^{15}N anomaly records into the surface nitrate concentration records, we use a ϵ_{AZ} value of 6‰ and assume that ϵ_{AZ} in the AZ has not changed over the past 40 kyr.

3. Subantarctic zone summertime surface nitrate concentration since 40 kyr

In the SAZ, the coral and foraminifera records also show 4-5‰ higher $\delta^{15}N_{integrated}$ during the LGM than the late Holocene (Fig. 3b). As for the AZ above, we consider here the possibility of changes in $\delta^{15}N_{initial}$ and nitrate assimilation isotope effect and their role in the 4-5‰ higher LGM $\delta^{15}N_{integrated}$ in the SAZ.

In contrast to the AZ, the modern SAZ thermocline water has two primary sources of nitrate and at least three sources of water. First, Ekman transport carries AZ surface water into the SAZ, and this water contains the nitrate remaining from nitrate assimilation in the AZ (18). This nitrate enters the SAZ at the surface, but it is mixed throughout the deep wintertime SAZ mixed layer,

including the depths of Subantarctic Mode Water. Second, the SAZ thermocline exchanges waters with the low latitude upper ocean. This water has a very low nitrate concentration and effectively dilutes the nitrate in the SAZ thermocline (46). Third, diapycnal mixing of the SAZ thermocline with underlying AAIW and UCDW incorporates nitrate with a high concentration (~35 μM) and relatively low $\delta^{15}N$ (~5.5‰). It has been estimated that the Ekman transport contributes to 60-70% of the SAZ thermocline nitrate in the modern ocean, with diapycnal mixing making up the remaining 30-40% (47).

We use a three end-member mixing model to simulate the mean concentration and $\delta^{15}N$ of the gross nitrate supply to the SAZ thermocline/wintertime mixed layer. Because the low latitude water contains no nitrate and because we have no reason to expect its contribution of water to vary relative the contribution from UCDW, we combine the low latitude water end-member with the UCDW end-member. In this way, the three end-member mixing model is simplified to a two end-member mixing model. Thus, we use the following proportions of water from the three sources described above: 60% from the Ekman transport and 40% from the combined UCDW and low latitude water.

Equations (6) and (7) describe the mixing results of the SAZ thermocline nitrate:

(6) $[NO_3^-]_{SAZ-thermocline} = [NO_3^-]_{UCDW} \times f_{AZ} \times b + [NO_3^-]_{mixedUCDW} \times (1-b)$

(7) $\delta^{15}N_{SAZ-thermocline}$

$$= \delta^{15}N_{AZ[NO_3^-]} \times \frac{[NO_3^-]_{UCDW} \times f_{AZ} \times b}{[NO_3^-]_{SAZ-thermocline}}$$

$$+ \delta^{15}N_{mixedUCDW} \times \frac{[NO_3^-]_{mixedUCDW} \times (1-b)}{[NO_3^-]_{SAZ-thermocline}}$$

where $[NO_3^-]_{SAZ-thermocline}$ is the nitrate concentration in the SAZ thermocline; b is the SAZ water fraction from the AZ (set to a constant value of 0.6; (47); $[NO_3^-]_{mixedUCDW}$ is the UCDW nitrate concentration after mixing with low latitude water (set to a constant value of 18 μM; (17, 18)); $\delta^{15}N_{mixedUCDW}$ is the δ^{15}N of the UCDW nitrate input to the SAZ (set to a constant value of 5.5‰; (17, 18)).

This mixing yields a modern SAZ thermocline/winter mixed layer nitrate concentration of ~20 μM, which is assumed to be drawn down to ~10 μM by nitrate assimilation in the SAZ (18). Holding these water mixing proportions constant, we estimate the changing SAZ thermocline nitrate concentration from 40 kyr to the present (Fig. S6). One clear over-simplification is that summertime AZ conditions are used to calculate the year-round nitrate concentration coming from the AZ. A biogeochemical box model of the AZ suggests the winter-to-summer nitrate concentration decline in the AZ was very weak during the LGM (Kemeny, 2015 Thesis), such that our approach is a reasonable simplification so far as the effect of the AZ on the SAZ nitrate concentration is concerned.

The reconstructed nitrate concentration for the gross nitrate supply to the SAZ provides the initial nitrate concentration for the Rayleigh model calculation (Equation (8) and (9)),

(8) $\delta^{15}N_{SAZ-integrated} = \delta^{15}N_{SAZ-thermocline} + \epsilon_{SAZ} \times \frac{f_{SAZ} \times \ln f_{SAZ}}{1 - f_{SAZ}}$

(9) $[NO_3^-]_{SAZ} = [NO_3^-]_{SAZ-thermocline} \times f_{SAZ}$

where ϵ_{SAZ} is the isotope effect of nitrate assimilation in the SAZ (set to a constant value of 8.5‰; (18)); and f_{SAZ} is the fraction of residual nitrate in the SAZ surface (with a modern value of 0.5).

The same mixing model also provides a reconstruction of the $\delta^{15}N$ of the gross nitrate supply to the SAZ (Equation (7) and Fig. S6). Fig. S8b uses this as well as the calculated nitrate concentration described above as the initial nitrate $\delta^{15}N$ and concentration for the Rayleigh model calculation. The $\delta^{15}N$ of the gross nitrate supply to the SAZ from all sources tends to decrease under the LGM case of nearly complete nitrate consumption in the AZ (Fig. S6, S7). Relative to UCDW, the AZ surface elevates the $\delta^{15}N$ of the nitrate supply to the SAZ. When AZ nitrate concentration is very low, it can no longer play this role, and the $\delta^{15}N$ of the nitrate supply to the SAZ collapses on the $\delta^{15}N$ of UCDW nitrate.

The calculation of the $\delta^{15}N$ of the nitrate supply to the SAZ is more uncertain than that of the concentration of the nitrate supply. A high degree of nitrate consumption in the AZ surface during the LGM would by itself raise the $\delta^{15}N$ of the nitrate to be transported northward into the SAZ. However, the resulting low concentration of nitrate in the summer AZ means that its wintertime mixing with underlying water could erase much of this $\delta^{15}N$ elevation. Accounting for such dilution effects is inherently uncertain. Nevertheless, in the calculations, the AZ is not a

major nitrate source to the SAZ during the LGM, and so the $\delta^{15}N$ of this minor nitrate source has little effect on the $\delta^{15}N$ of the nitrate supply to the SAZ at this time.

Similar to the AZ, a change in ϵ_{SAZ} would lead to changes in $\delta^{15}N_{SAZ-integrated}$. However, in comparison with the AZ, a given change in ϵ_{SAZ} will contribute less to the higher LGM $\delta^{15}N_{SAZ-integrated}$ in the SAZ because the average surface nitrate consumption is already at ~50% in modern SAZ (Fig. S5).

Figure Captions

Fig. S1. Nitrogen isotopes of corals from Tasmania (a) and Drake Passage (b), with the colors indicating collection depths of each coral. The error bars are calculated from 2-3 replicates from the same sample.

Fig. S2. Tasmania coral $\delta^{15}N$ variation on single septa along the growth direction. Each symbol indicates one individual coral (filled symbol: late Holocene corals; empty symbol: Bølling-Allerød corals).

Fig. S3. Box plots of coral $\delta^{15}N$ for each 5 kyr bin (except for 20-40 kyr) and *p* values of each two adjacent groups based on Mann-Whitney U test (Wilcoxon rank-sum test).

Fig. S4. Comparison of coral $\delta^{15}N$ and N content, with samples colored based on ages. If there is any tendency in N content as a function of age, it is of increasing N content with age, the opposite expectation if there were N loss with age. There is a lack a lack of correlation between N content and coral $\delta^{15}N$ (r^2 values shown in upper left).

Fig. S5. Contours of the $\boldsymbol{\delta^{15}N_{AZ-integrated}}$ as a function of $\boldsymbol{\varepsilon}$ and $(\mathbf{1}-\boldsymbol{f})$, based on the Rayleigh model (initial nitrate $\delta^{15}N$ of 5‰). The downward convergence of isolines shows that $\boldsymbol{\delta^{15}N_{AZ-integrated}}$ is less sensitive to the isotope effect of nitrate assimilation than the surface nitrate consumption when the surface nitrate consumption is higher than 50%.

Fig. S6. Calculated SAZ thermocline nitrate concentration and $\delta^{15}N$ in our model. Changes in both the concentration and the $\delta^{15}N$ of SAZ thermocline nitrate are included in the calculated SAZ summertime surface nitrate concentration plotted in Fig. S8b.

Fig. S7. A schematic showing the impact of AZ processes on the SAZ nitrate concentration and $\delta^{15}N$. (a) In the modern ocean, the surface nitrate concentration is high in the AZ, and the northward Ekman transport transfers a large amount of nitrate to the SAZ, contributing to 60-70% of the gross nitrate supply to the SAZ. (b) During the last glacial maximum, the surface nitrate concentration is low in the AZ, and the northward Ekman transport thus transfers less nitrate (but with higher $\delta^{15}N$) to the SAZ. Under these conditions, the dominant nitrate source in the SAZ is underlying UCDW.

Fig. S8. Comparison of coral $\delta^{15}N$ records with the sedimentary microfossil $\delta^{15}N$ records as in Fig. 3 and the calculated Southern Ocean summertime surface nitrate concentration. (a) Comparison of the Drake Passage AZ coral $\delta^{15}N$ mean record with the PS75/072-4 AZ diatom $\delta^{15}N$ record ($\delta^{15}N$ anomaly was calculated by subtracting the modern or core-top $\delta^{15}N$ values from each record) (13) and the calculated AZ summertime surface nitrate concentration over the past 40 kyr (*SI text*); and (b) comparison of the SAZ coral $\delta^{15}N$ records with the ODP Site 1090 SAZ foraminifera $\delta^{15}N$ record (12) and the calculated SAZ summertime surface nitrate concentration with correction for SAZ thermocline nitrate concentration and $\delta^{15}N$ changes (SI text and Fig. S6 and S7).

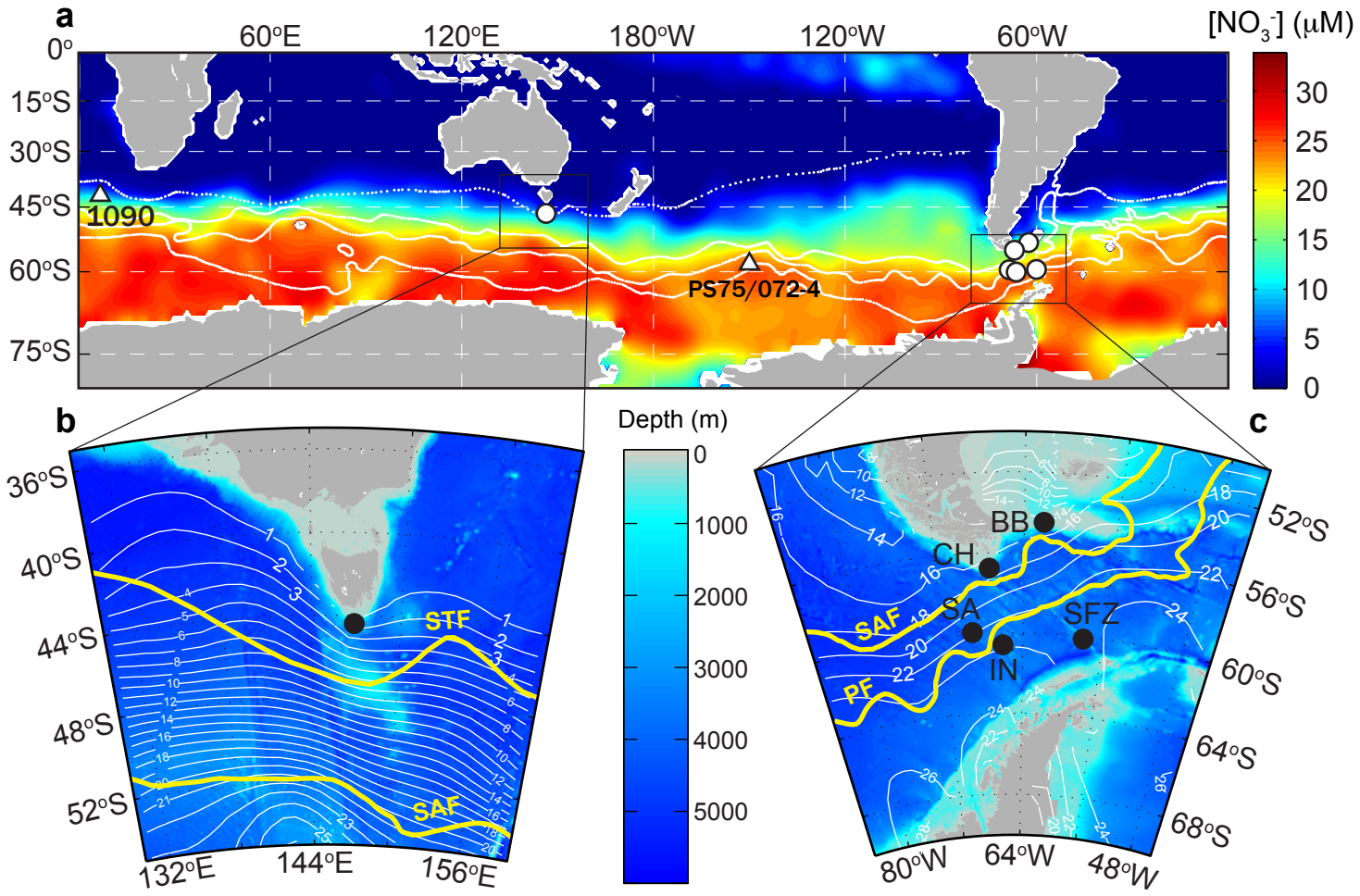
a
[NO3-] (µM)
0°
15°S
30°S
45°S
60°S
75°S
60°E
120°E
180°W
120°W
60°W
30
25
20
15
10
5
0
1090
PS75/072-4
b
c
Depth (m)
0
1000
2000
3000
4000
5000
36°S
40°S
44°S
48°S
52°S
132°E
144°E
156°E
STF
SAF
80°W
64°W
48°W
52°S
56°S
60°S
64°S
68°S
BB
CH
SA
IN
SFZ
SAF
PF

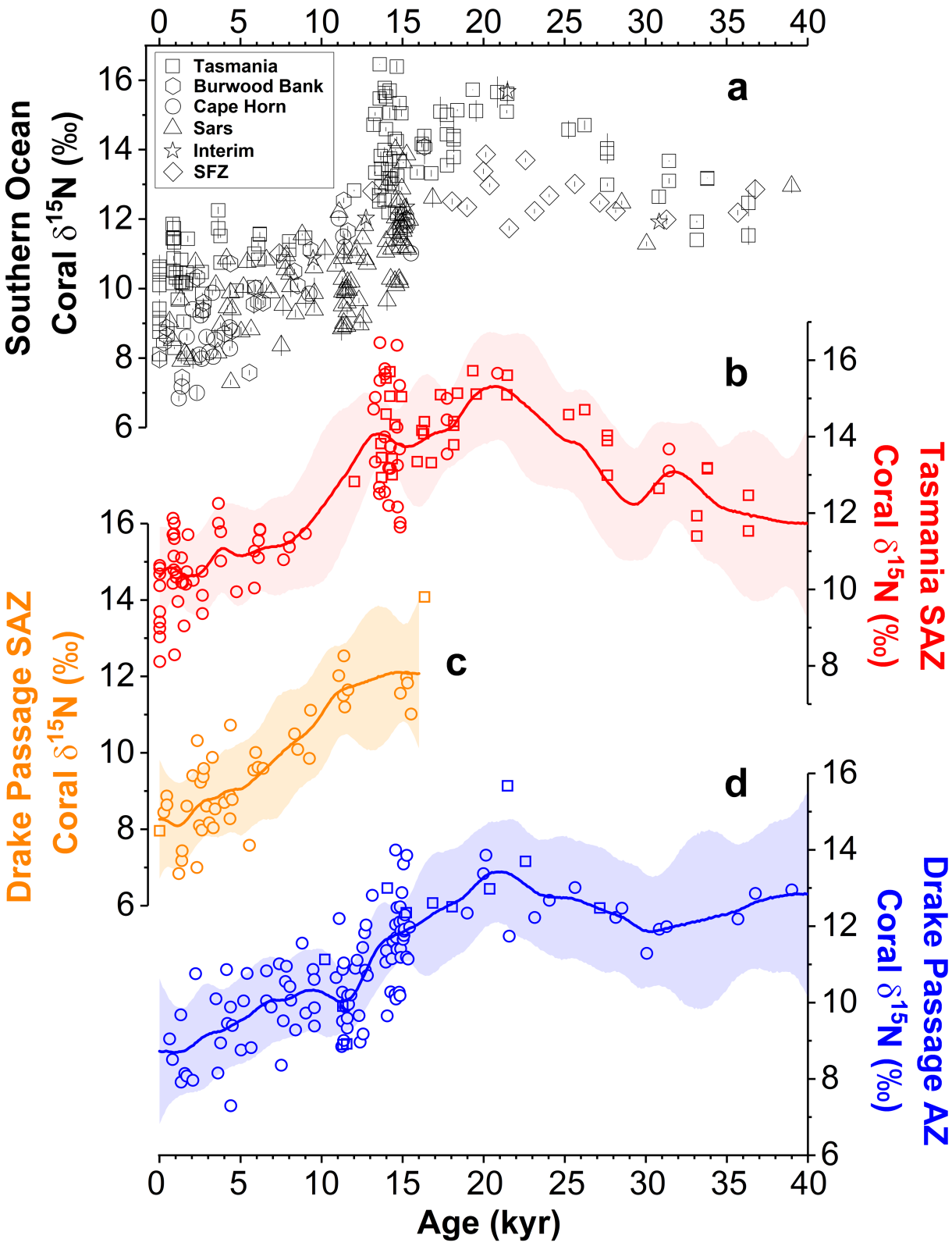
Tasmania
Burwood Bank
Cape Horn
Sars
Interim
SFZ
a
b
c
d
Southern Ocean
Coral δ15N (‰)
Tasmania SAZ
Coral δ15N (‰)
Drake Passage SAZ
Coral δ15N (‰)
Drake Passage AZ
Coral δ15N (‰)
Age (kyr)
0
5
10
15
20
25
30
35
40
6
8
10
12
14
16

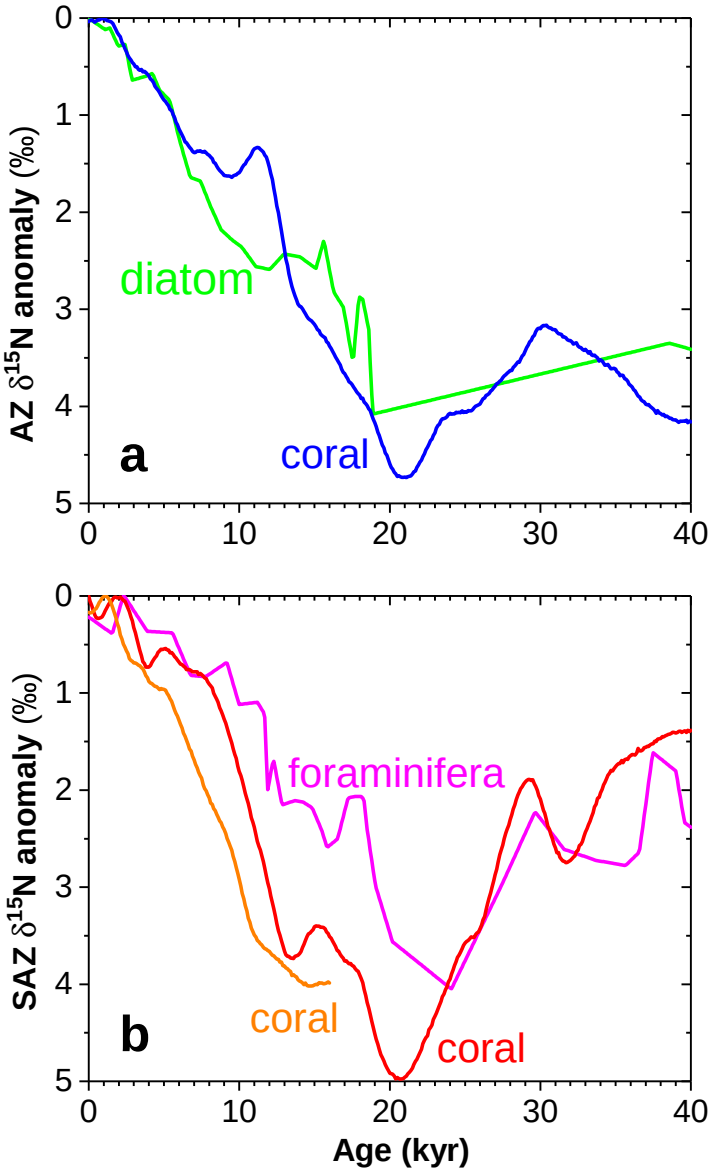
AZ δ15N anomaly (‰)
diatom
coral
a
SAZ δ15N anomaly (‰)
foraminifera
coral
coral
b
Age (kyr)
0
1
2
3
4
5
0
10
20
30
40

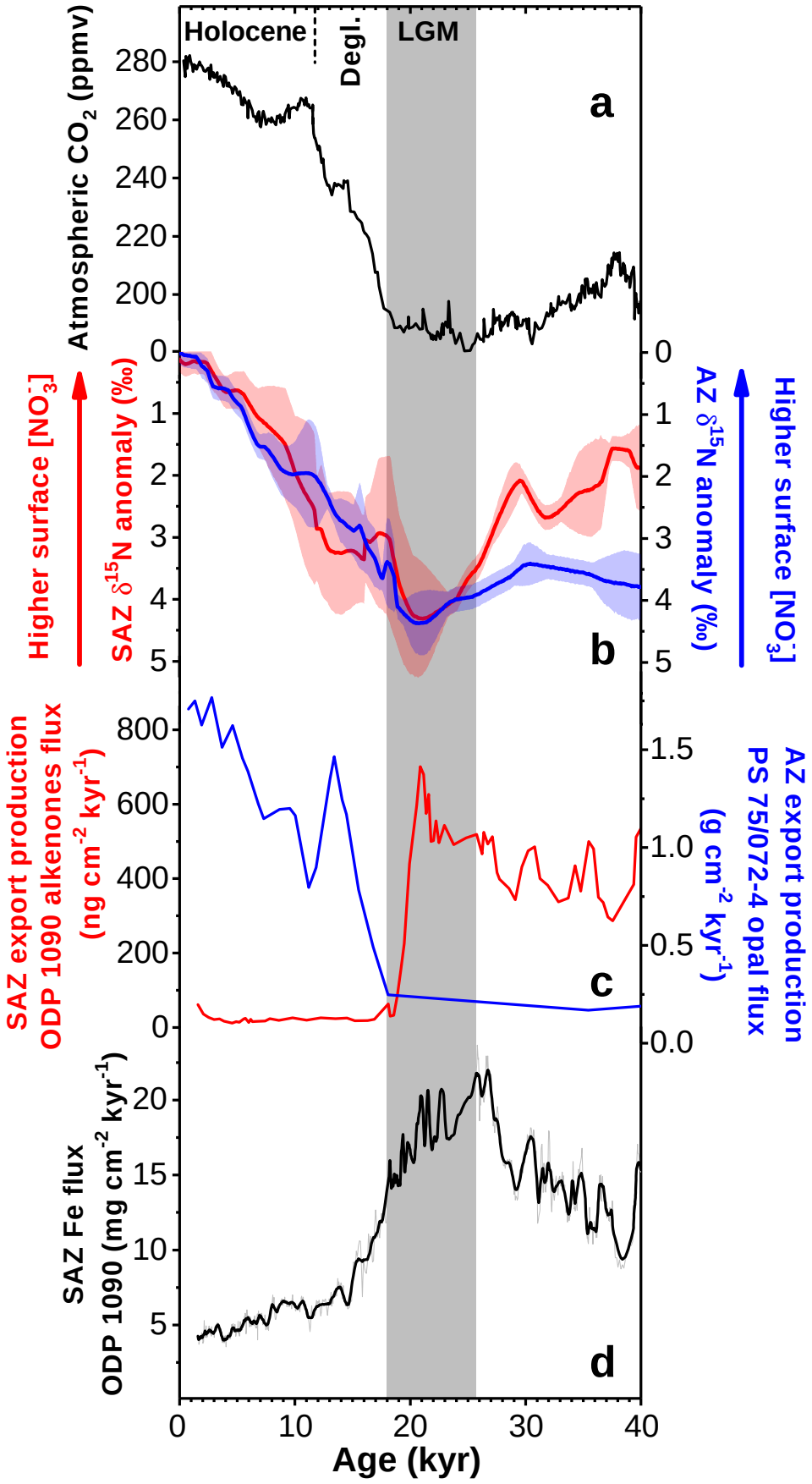
Holocene
Degl.
LGM
a
b
c
d
Atmospheric CO2 (ppmv)
Higher surface [NO3-]
SAZ δ15N anomaly (‰)
AZ δ15N anomaly (‰)
Higher surface [NO3-]
SAZ export production
ODP 1090 alkenones flux
(ng cm-2 kyr-1)
AZ export production
PS 75/072-4 opal flux
(g cm-2 kyr-1)
SAZ Fe flux
ODP 1090 (mg cm-2 kyr-1)
Age (kyr)

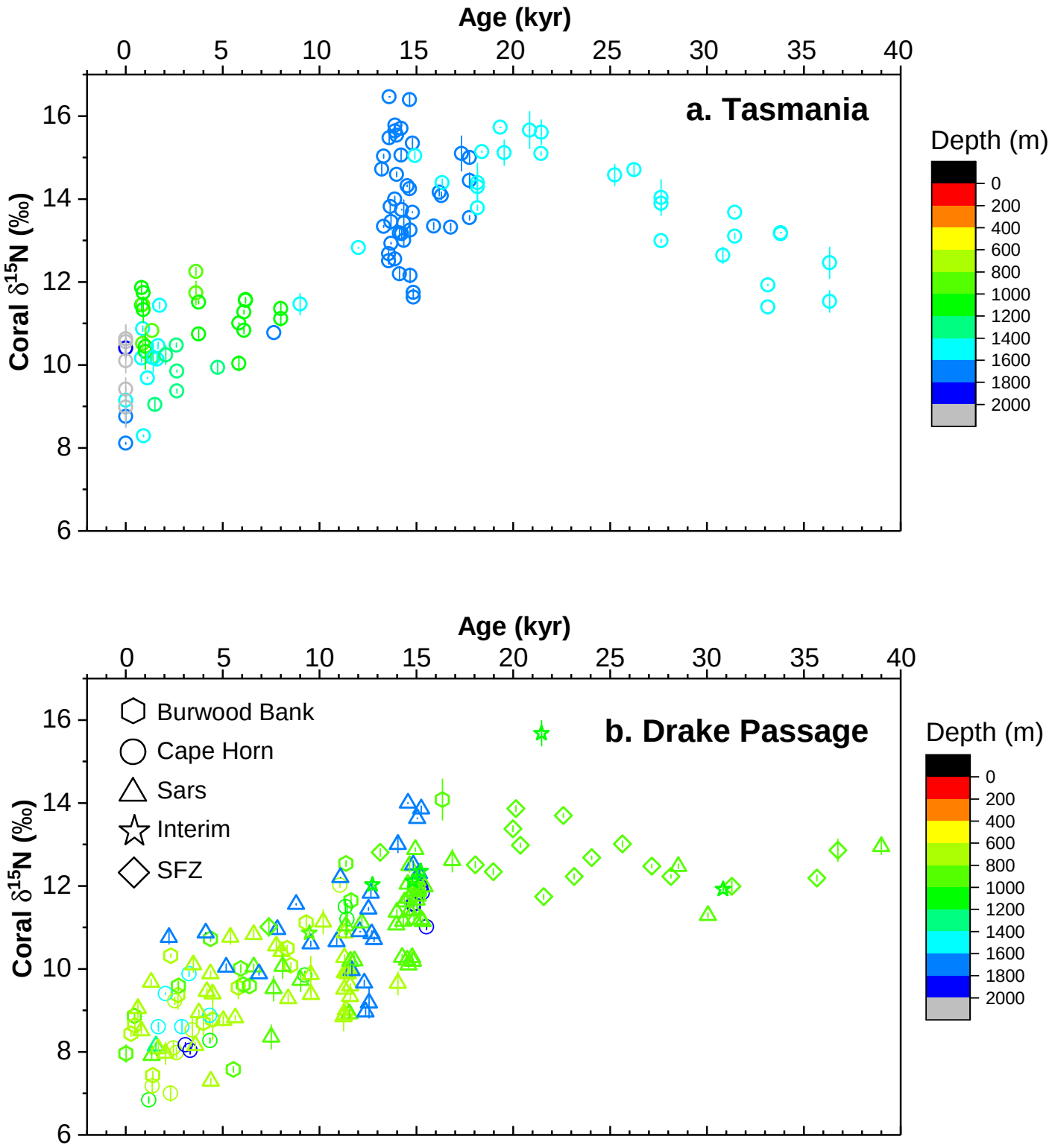
Age (kyr)
0
5
10
15
20
25
30
35
40
a. Tasmania
Coral δ15N (‰)
6
8
10
12
14
16
Depth (m)
0
200
400
600
800
1000
1200
1400
1600
1800
2000
Age (kyr)
b. Drake Passage
Burwood Bank
Cape Horn
Sars
Interim
SFZ
Coral δ15N (‰)
Depth (m)

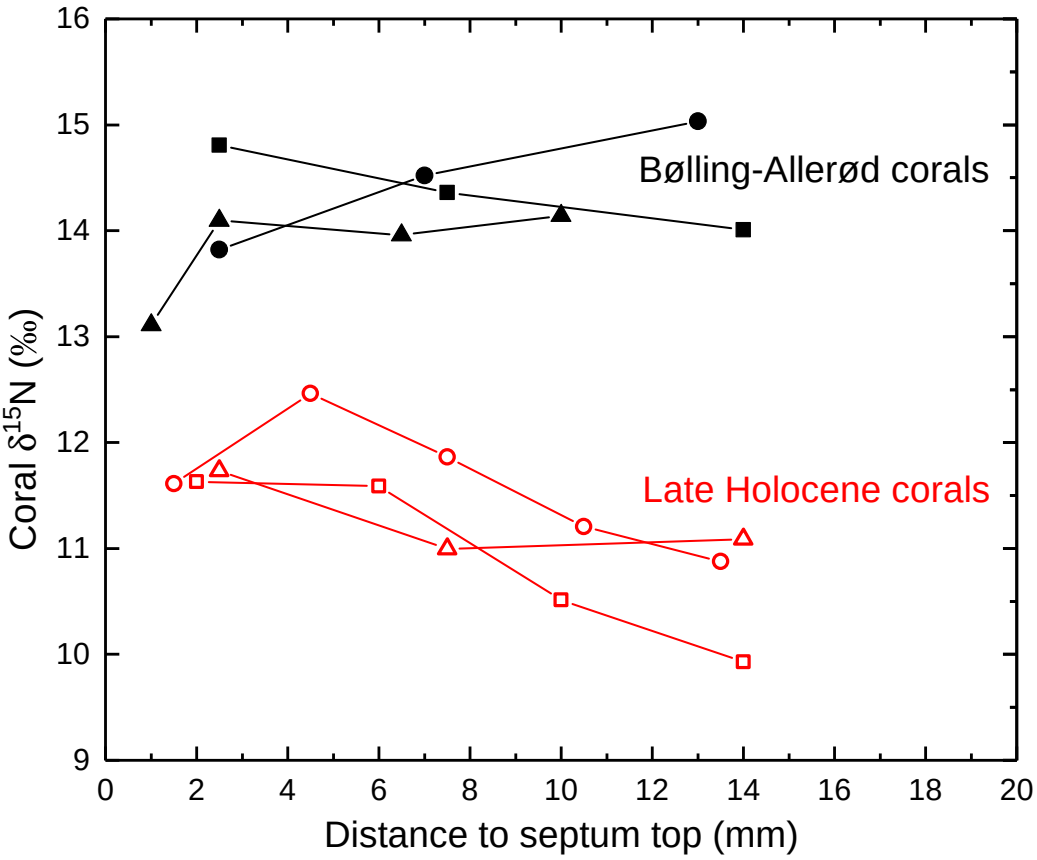
Bølling-Allerød corals
Late Holocene corals
Coral δ15N (‰)
Distance to septum top (mm)
16
15
14
13
12
11
10
9
0
2
4
6
8
10
12
14
16
18
20

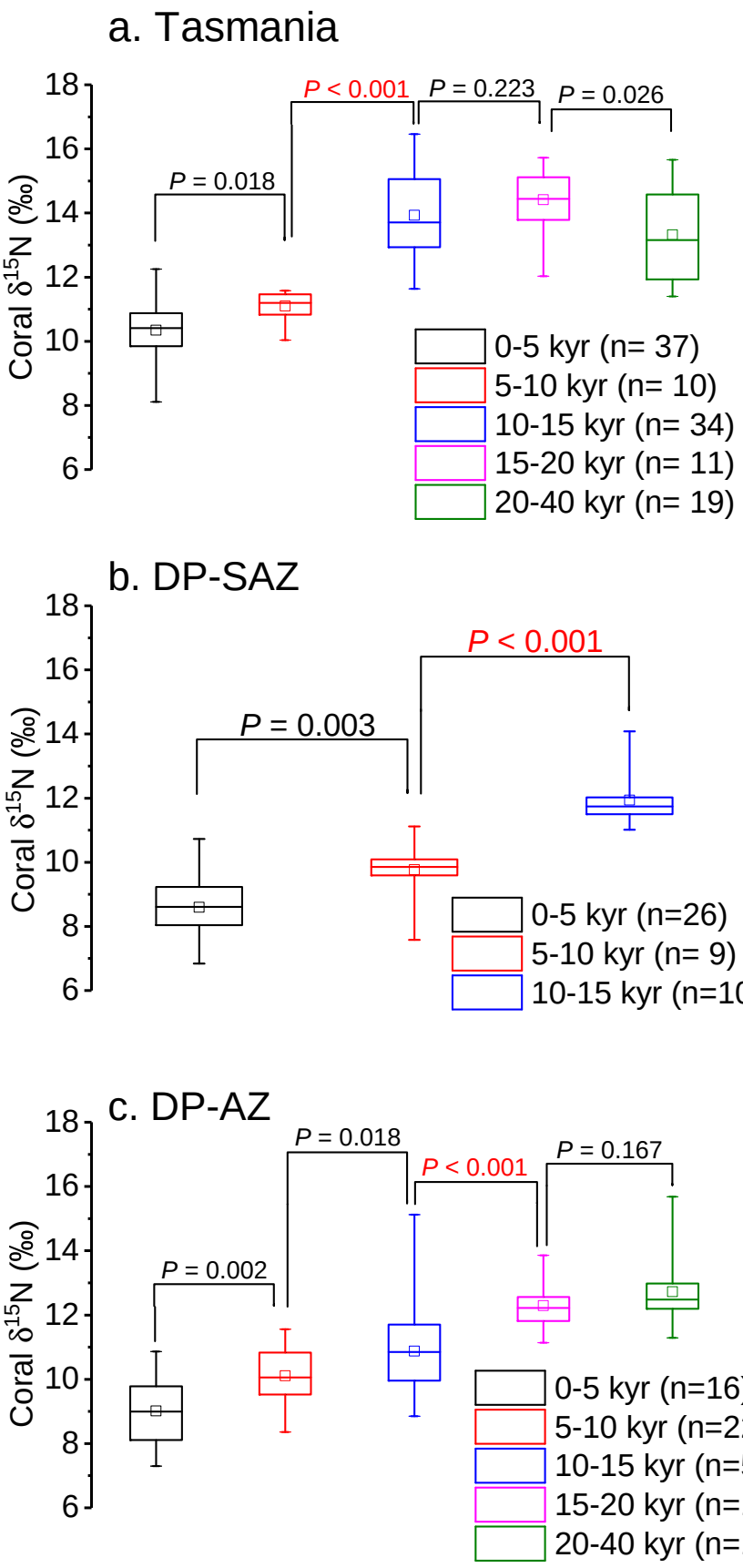
a. Tasmania
Coral δ15N (‰)
18
16
14
12
10
8
6
P = 0.018
P < 0.001
P = 0.223
P = 0.026
0-5 kyr (n= 37)
5-10 kyr (n= 10)
10-15 kyr (n= 34)
15-20 kyr (n= 11)
20-40 kyr (n= 19)
b. DP-SAZ
Coral δ15N (‰)
P = 0.003
P < 0.001
0-5 kyr (n=26)
5-10 kyr (n= 9)
10-15 kyr (n=10)
c. DP-AZ
Coral δ15N (‰)
P = 0.002
P = 0.018
P < 0.001
P = 0.167
0-5 kyr (n=16)
5-10 kyr (n=22)
10-15 kyr (n=53)
15-20 kyr (n=16)
20-40 kyr (n=17)

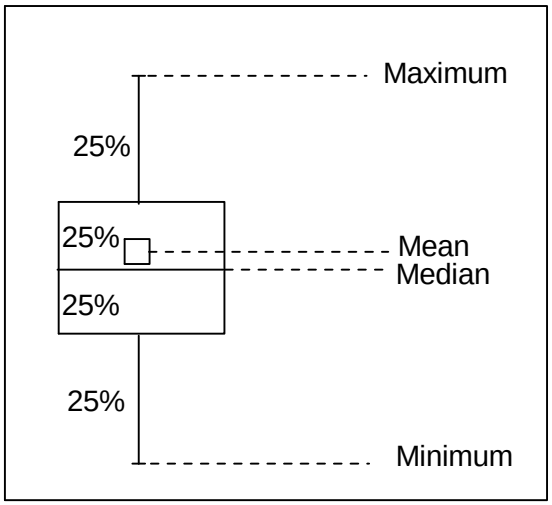
Maximum
25%
25%
Mean
Median
25%
25%
Minimum

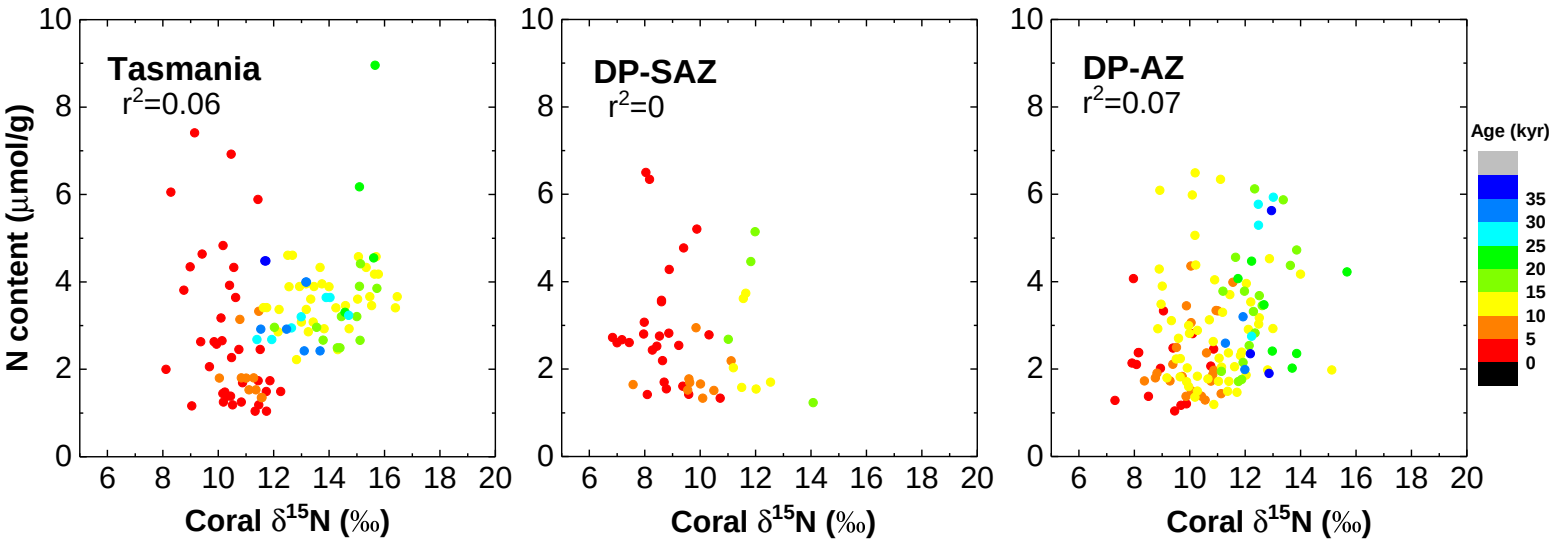
Tasmania
r2=0.06
DP-SAZ
r2=0
DP-AZ
r2=0.07
N content (µmol/g)
Coral δ15N (‰)
Age (kyr)
35
30
25
20
15
10
5
0

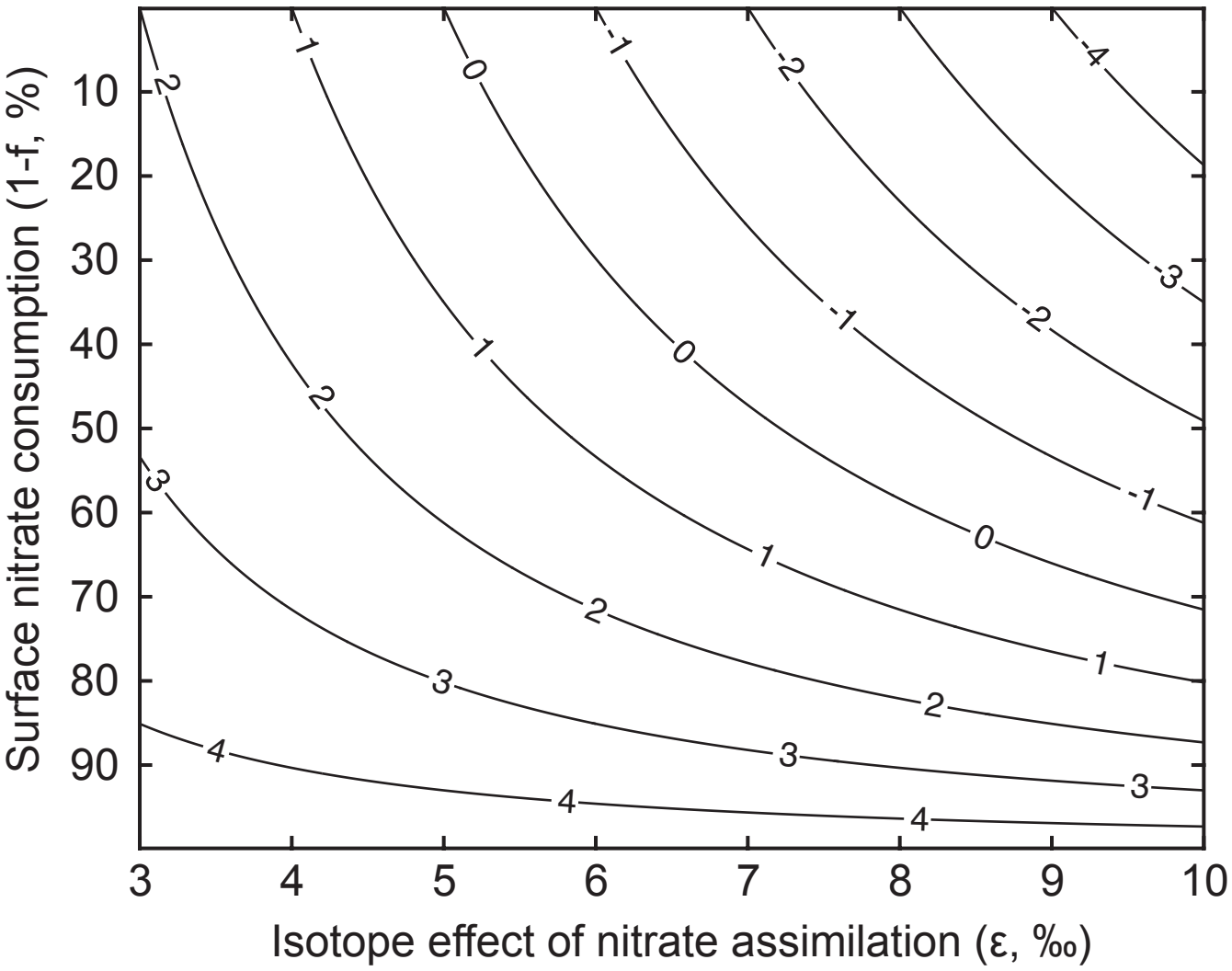
Surface nitrate consumption (1-f, %)
10
20
30
40
50
60
70
80
90
3
4
5
6
7
8
9
10
Isotope effect of nitrate assimilation (ε, ‰)
2
1
0
-1
-2
-4
-3
1
2
3
0
-1
1
2
3
4
2
3
4

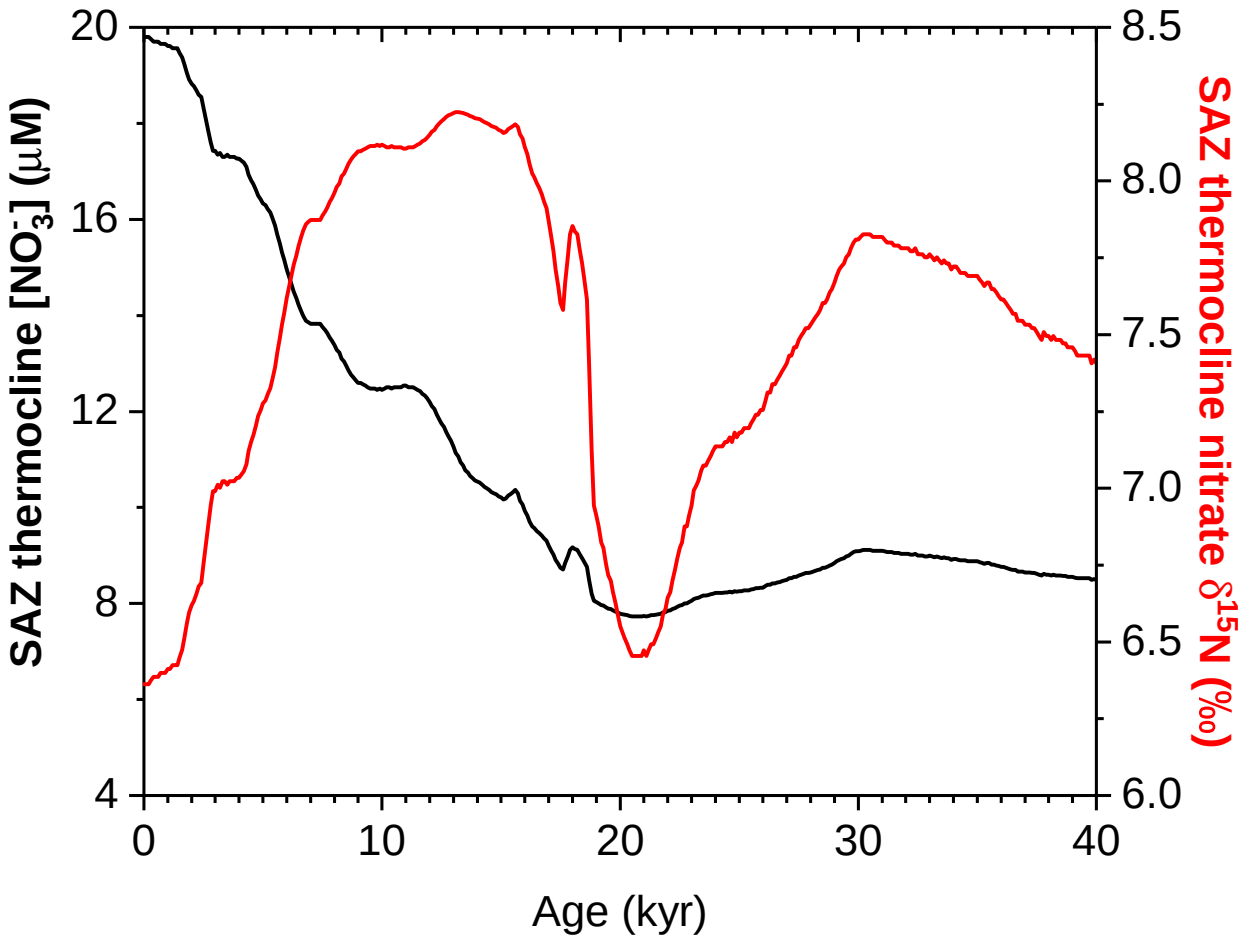
SAZ thermocline [NO3-] (μM)
SAZ thermocline nitrate δ15N (‰)
Age (kyr)
20
16
12
8
4
8.5
8.0
7.5
7.0
6.5
6.0
0
10
20
30
40

a. Modern ocean

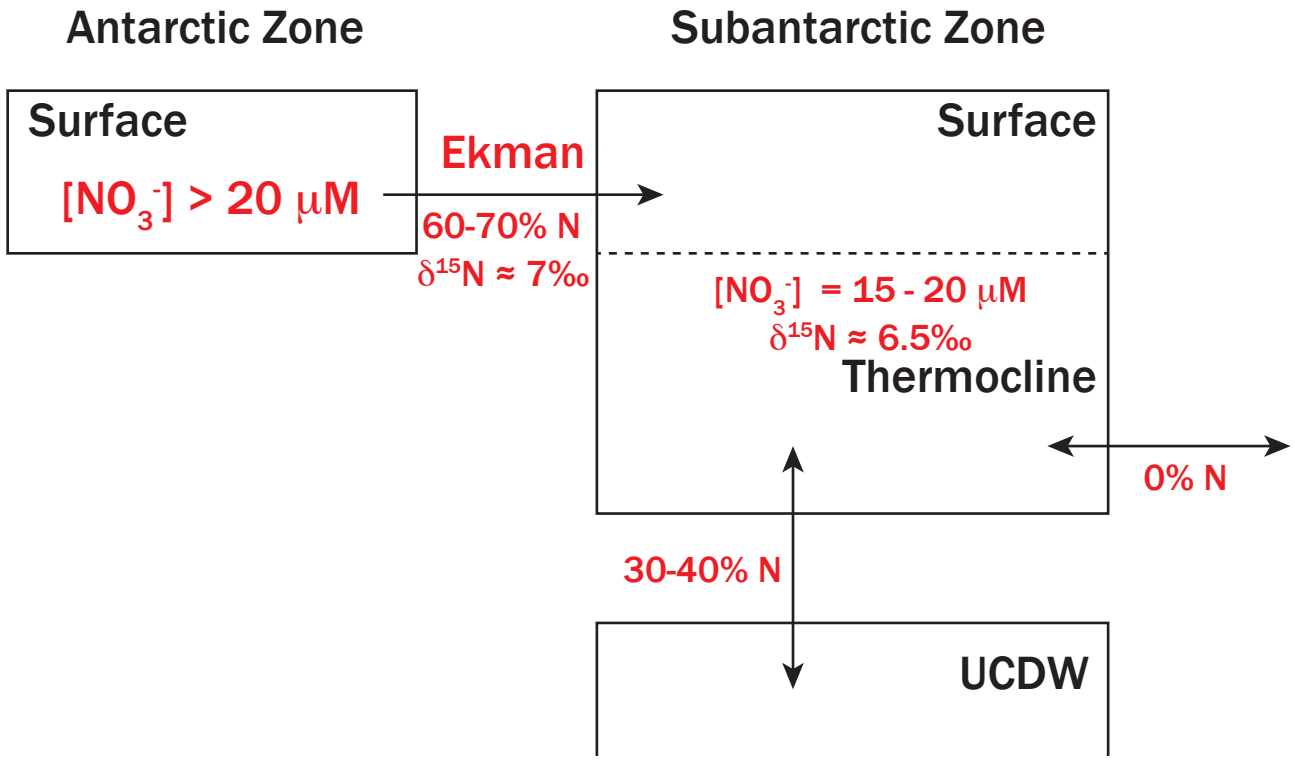

b. Last glacial maximum

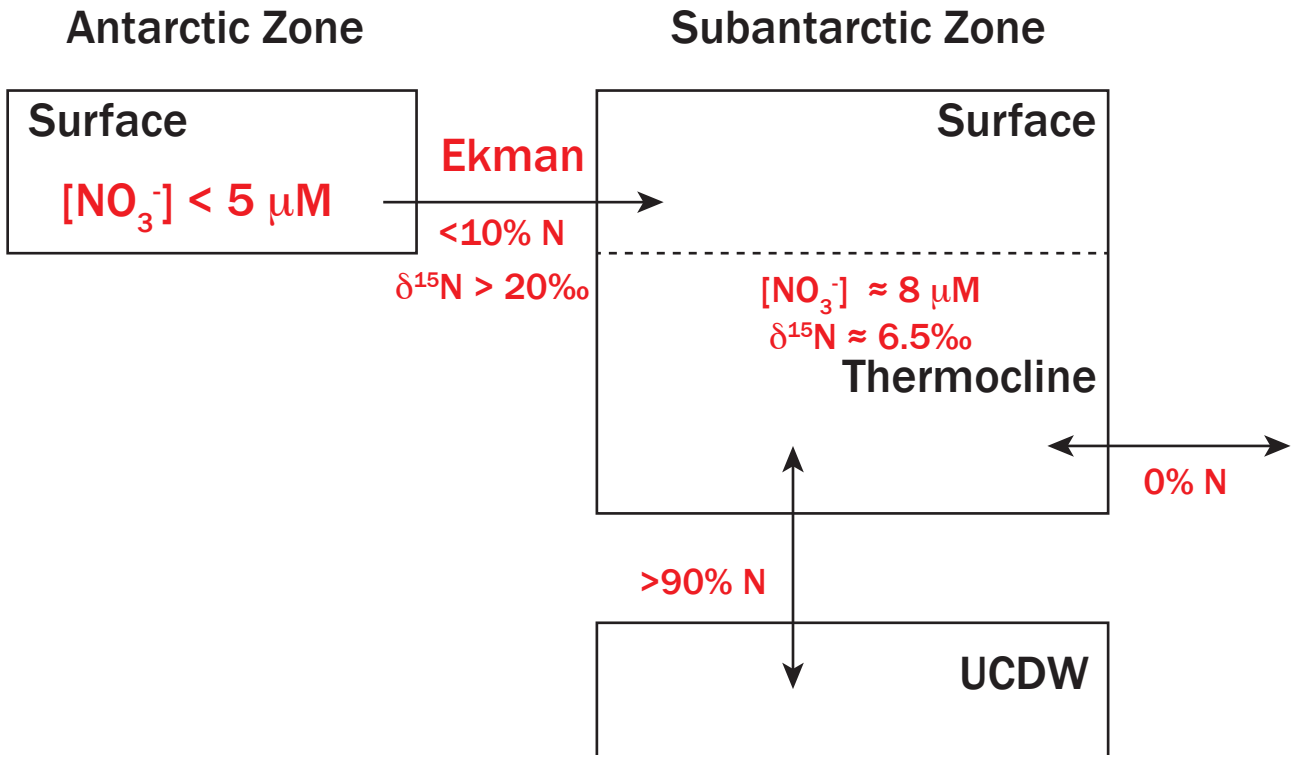

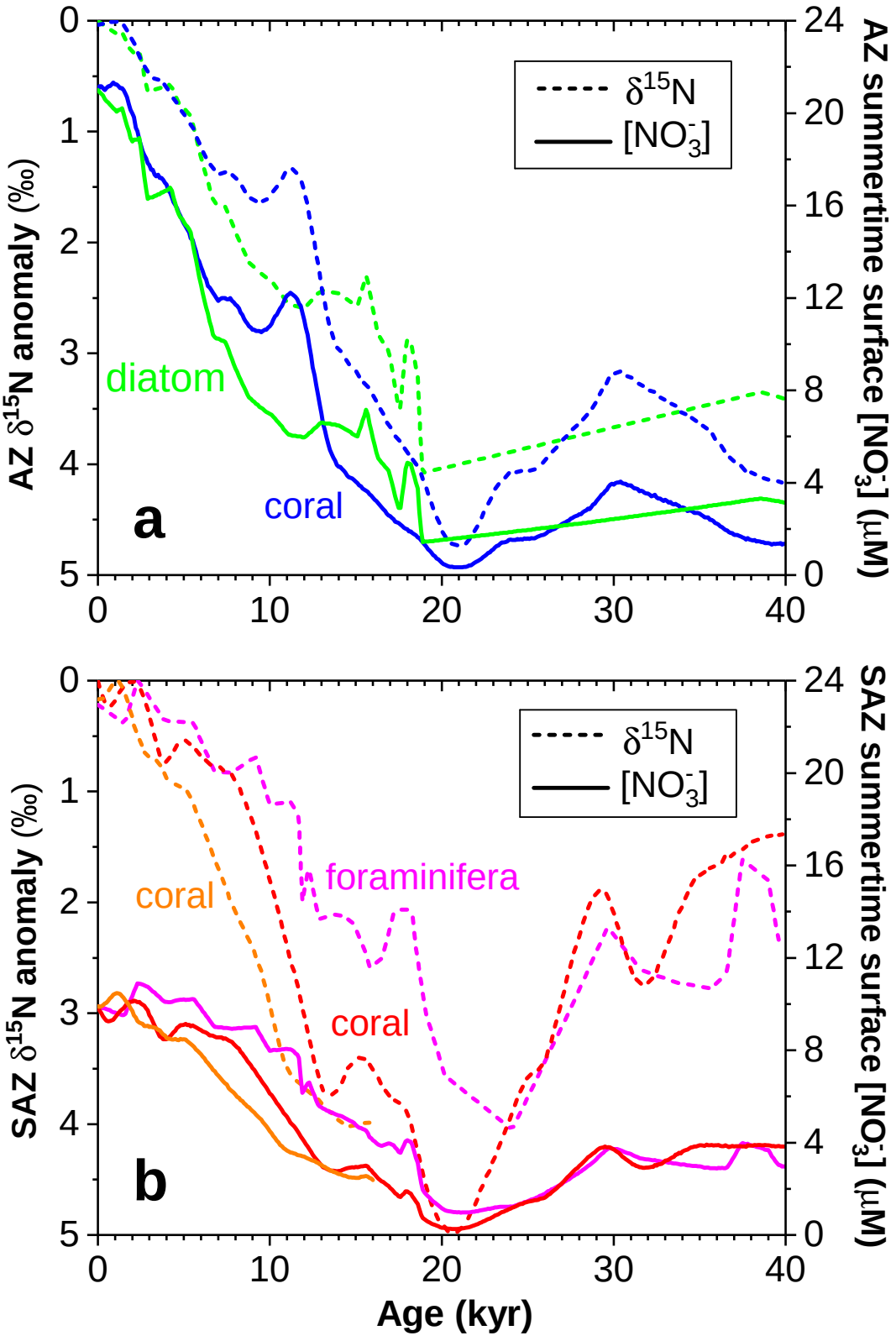
AZ δ15N anomaly (‰)
AZ summertime surface [NO3-] (μM)
δ15N
[NO3-]
diatom
coral
a
SAZ δ15N anomaly (‰)
SAZ summertime surface [NO3-] (μM)
coral
foraminifera
coral
b
Age (kyr)

Table S1 Calendar ages and nitrogen isotopes of Tasmania corals in this study.

Sample ID	Depth (m)	Latitude (°N)	Longitude (°E)	U-Th Age (year)	^{14}C-based calendar age after correction (year)	Final calendar age (year)	Age error (1sd)	$\delta^{15}N$ (‰)	1sd
4-13-MP1-2	1460	-44.32	147.27	nd	0	0	500	9.15	0.17
4-13-MP3	1616	-44.39	147.26	nd	0	0	500	8.76	0.24
4-13-MP4	1898	-44.38	147.26	nd	0	0	500	10.41	0.23
4-13-MP5	2040	-44.39	147.27	nd	0	0	500	10.10	0.29
4-13-MP6-7	2090	-44.31	147.45	nd	0	0	500	10.63	0.33
4-13-MP9-10	2193	-44.31	147.45	nd	0	0	500	10.56	0.41
CMP-5 & 6	2193	-44.50	147.47	nd	0	0	500	8.99	0.49
CMP-7 & 8	2395	-44.50	147.47	nd	0	0	500	9.42	0.27
MP-SOI-I10	1616	-44.39	147.26	nd	0	0	500	8.11	0.02
MP-SOI-I4	1500	-44.32	147.27	nd	812	812	500	10.16	0.10
MP-SOI-F10-A	1184	-44.24	147.12	nd	818	818	500	11.44	0.12
MP-SOI-F10-B	1184	-44.24	147.12	nd	818	818	500	11.87	0.17
MP-SOI-F02-A	899	-44.26	147.11	nd	872	872	500	10.52	0.19
MP-SOI-F02-B	899	-44.26	147.11	nd	872	872	500	11.46	0.00
MP-SOI-I1	1454	-44.30	147.39	nd	873	873	500	10.87	0.06
MP-SOI-F11-A	1184	-44.24	147.12	nd	897	897	500	11.74	0.00
MP-SOI-F11-B	1184	-44.24	147.12	nd	897	897	500	11.33	0.31
MP-SOI-I9	1548	-44.32	147.26	nd	914	914	500	8.29	0.03
MP-SOI-F12-A	1184	-44.24	147.12	nd	1014	1014	500	10.32	0.42
MP-SOI-F12-B	1184	-44.24	147.12	nd	1014	1014	500	10.45	0.07
MP-SOI-I7	1548	-44.32	147.26	nd	1125	1125	500	9.69	0.01
MP-SOI-F03-A	899	-44.26	147.11	nd	1345	1345	500	10.83	0.00
MP-SOI-F03-B	899	-44.26	147.11	nd	1345	1345	500	10.19	0.08
MP-SOI-I6	1548	-44.32	147.26	nd	1418	1418	500	10.17	0.35
MP-SOI-H02	1305	-44.33	146.89	nd	1498	1498	500	9.05	0.15
MP-SOI-I5	1523	-44.35	146.89	nd	1614	1614	500	10.14	0.13
MP-SOI-I3	1460	-44.32	147.27	nd	1670	1670	500	10.46	0.08
MP-SOI-I8	1548	-44.32	147.26	nd	1747	1747	500	11.44	0.08
MP-SOI-H03	1305	-44.33	146.89	nd	2064	2064	500	10.24	0.22
MP-SOI-H04	1346	-44.32	147.27	nd	2613	2613	500	10.48	0.05
MP-SOI-F14-A	1240	-44.24	147.12	nd	2635	2635	500	9.85	0.03
MP-SOI-F14-B	1240	-44.24	147.12	nd	2635	2635	500	9.37	0.05
MP-SOI-F14-A	899	-44.26	147.11	nd	3625	3625	500	12.25	0.10
MP-SOI-F14-B	899	-44.26	147.11	nd	3625	3625	500	11.74	0.28
MP-SOI-F14-A	1060	-44.25	147.12	nd	3766	3766	500	11.51	0.04
MP-SOI-F14-B	1060	-44.25	147.12	nd	3766	3766	500	10.75	0.11
MP-SOI-F14	1397	-44.32	147.27	nd	4740	4740	500	9.94	0.16
MP-SOI-F14-A	1060	-44.25	147.12	nd	5843	5843	500	10.04	0.18
MP-SOI-F14-B	1060	-44.25	147.12	nd	5843	5843	500	11.01	0.01
MP-SOI-F14-A	1060	-44.25	147.12	nd	6096	6096	500	10.83	0.08

MP-SOI-F14-B	1060	-44.25	147.12	nd	6096	6096	500	11.28	0.04
MP-SOI-F14-A	1060	-44.25	147.12	nd	6185	6185	500	11.56	0.07
MP-SOI-F14-B	1060	-44.25	147.12	nd	6185	6185	500	11.58	0.01
MP-SOI-F14	1657	-45.14	146.98	nd	7644	7644	500	10.78	0.00
MP-SOI-F14-A	1184	-44.24	147.12	nd	8000	8000	500	11.11	0.18
MP-SOI-F14-B	1184	-44.24	147.12	nd	8000	8000	500	11.36	0.13
MP-SOI-F14	1454	-44.30	147.39	nd	8993	8993	500	11.47	0.26
MP-SOI-F14	1448	-44.39	147.25	12010	11894	12010	67	12.83	0.02
MP-SOI-F14-A	1680	-44.39	147.26	nd	13208	13208	500	14.72	0.17
MP-SOI-F14-B	1680	-44.39	147.26	13647	13208	13647	78	13.82	0.12
MP-SOI-F14-A	1680	-44.39	147.26	nd	13308	13308	500	13.34	0.03
MP-SOI-F14-B	1680	-44.39	147.26	nd	13308	13308	500	15.03	0.05
MP-SOI-F14-A	1748	-44.39	147.26	nd	13564	13564	500	12.68	0.07
MP-SOI-F14-B	1748	-44.39	147.26	nd	13564	13564	500	12.51	0.08
MP-SOI-F14-A	1680	-44.39	147.26	nd	13591	13591	500	16.46	0.00
MP-SOI-F14-B	1680	-44.39	147.26	nd	13591	13591	500	15.47	0.13
MP-SOI-F14-A	1680	-44.39	147.26	13691	13653	13691	325	13.45	0.20
MP-SOI-F14-B	1680	-44.39	147.26	13691	13653	13691	325	12.93	0.02
MP-SOI-F14-A	1748	-44.39	147.26	nd	13882	13882	500	14.00	0.07
MP-SOI-F14-B	1748	-44.39	147.26	nd	13882	13882	500	12.55	0.14
MP-SOI-F14-A	1680	-44.39	147.26	nd	13898	13898	500	15.64	0.19
MP-SOI-F14-B	1680	-44.39	147.26	nd	13898	13898	500	15.78	0.04
MP-SOI-F14-A	1680	-44.39	147.26	14208	14092	14208	84	15.06	0.15
MP-SOI-F14-B	1680	-44.39	147.26	14208	14092	14208	84	15.70	0.09
MP-SOI-F14-A	1748	-44.39	147.26	nd	14131	14131	500	13.18	0.17
MP-SOI-F14-B	1748	-44.39	147.26	nd	14131	14131	500	12.20	0.14
MP-SOI-F14-A	1680	-44.39	147.26	nd	14239	14239	500	13.17	0.17
MP-SOI-F14-B	1680	-44.39	147.26	nd	14239	14239	500	13.74	0.01
MP-SOI-F14-A	1748	-44.39	147.26	13974	14248	13974	59	14.59	0.06
MP-SOI-F14-B	1748	-44.39	147.26	13974	14248	13974	59	15.53	0.07
MP-SOI-F14-A	1748	-44.39	147.26	14349	14427	14349	46	13.42	0.55
MP-SOI-F14-B	1748	-44.39	147.26	14349	14427	14349	46	13.00	0.02
MP-SOI-F14-A	1680	-44.39	147.26	14520	14556	14520	53	14.31	0.02
MP-SOI-F14-A	1748	-44.39	147.26	nd	14645	14645	500	14.25	0.12
MP-SOI-F14-B	1748	-44.39	147.26	nd	14645	14645	500	16.39	0.15
MP-SOI-F14-A	1680	-44.39	147.26	nd	14674	14674	500	12.16	0.18
MP-SOI-F14-B	1680	-44.39	147.26	nd	14674	14674	500	13.25	0.18
MP-SOI-F14-A	1748	-44.39	147.26	nd	14805	14805	500	13.68	0.01
MP-SOI-F14-B	1748	-44.39	147.26	nd	14805	14805	500	15.34	0.12
MP-SOI-F14-A	1748	-44.39	147.26	nd	14841	14841	500	11.63	0.04
MP-SOI-F14-B	1748	-44.39	147.26	nd	14841	14841	500	11.75	0.09
MP-SOI-F14	1599	-44.39	147.26	14927	14565	14927	50	15.05	0.09
MP-SOI-F14	1748	-44.39	147.26	15892	15898	15892	64	13.35	0.09
MP-SOI-F14	1748	-44.39	147.26	16184	16052	16184	72	14.17	0.09

MP-SOI-F14	1748	-44.39	147.26	16294	15980	16294	74	14.08	0.09
MP-SOI-F14	1442	-44.39	147.26	16336	14796	16336	523	14.39	0.09
MP-SOI-F14	1689	-44.39	147.26	16770	16227	16770	66	13.32	0.09
MP-SOI-F14	1689	-44.39	147.26	17330	17484	17330	110	15.10	0.42
MP-SOI-F14-A	1748	-44.39	147.26	nd	17735	17735	500	15.00	0.13
MP-SOI-F14-B	1748	-44.39	147.26	nd	17735	17735	500	14.44	0.19
MP-SOI-F14	1748	-44.39	147.26	nd	17741	17741	500	13.55	0.05
MP-SOI-F14-A	1575	-44.32	147.26	18151	18035	18151	66	14.40	0.46
MP-SOI-F14-B	1575	-44.32	147.26	18151	18035	18151	66	14.30	0.33
MP-SOI-F14	1575	-44.32	147.26	18151	18035	18151	66	13.79	0.07
MP-SOI-F14	1523	-44.35	146.89	18379	18554	18379	38	15.14	0.02
MP-SOI-F14	1460	-44.32	147.27	19533	18688	19533	63	15.12	0.31
MP-SOI-F14	1460	-44.32	147.27	19326	19573	19326	58	15.73	0.00
MP-SOI-F14	1523	-44.35	146.89	nd	20849	20849	500	15.66	0.45
MP-SOI-F14	1460	-44.32	147.27	21453	21096	21453	57	15.61	0.30
MP-SOI-F14	1523	-44.35	146.89	21431	21354	21431	184	15.10	0.04
MP-SOI-F14	1500	-44.30	147.39	25241	24045	25241	143	14.58	0.25
MP-SOI-F14-A	1575	-44.32	147.26	27629	25040	27629	92	13.90	0.16
MP-SOI-F14-B	1575	-44.32	147.26	27629	25040	27629	92	14.04	0.43
MP-SOI-F14	1575	-44.32	147.26	27629	25040	27629	92	12.99	0.04
MP-SOI-F14	1575	-44.32	147.26	26233	25898	26233	56	14.71	0.13
MP-SOI-F14	1500	-44.30	147.39	30814	27442	30814	194	12.65	0.20
MP-SOI-F14-A	1575	-44.32	147.26	33150	29163	33150	1135	11.93	0.02
MP-SOI-F14-B	1575	-44.32	147.26	33150	29163	33150	1135	11.40	0.00
MP-SOI-F14-A	1500	-44.30	147.39	nd	31435	31435	500	13.10	0.07
MP-SOI-F14-B	1500	-44.30	147.39	nd	31435	31435	500	13.68	0.01
MP-SOI-F14-A	1575	-44.32	147.26	33803	32233	33803	132	13.19	0.00
MP-SOI-F14-B	1575	-44.32	147.26	33803	32233	33803	132	13.16	0.00
MP-SOI-F14-A	1575	-44.32	147.26	36338	34592	36338	189	12.47	0.38
MP-SOI-F14-B	1575	-44.32	147.26	36338	34592	36338	189	11.53	0.26
MP-SOI-F14-A	1575	-44.32	147.26	41479	38771	41479	107	11.68	0.00
MP-SOI-F14-B	1575	-44.32	147.26	41479	38771	41479	107	11.72	0.20

Table S2 Calendar age and nitrogen isotopes of Drake Passage corals in this study.

Sample ID	Location	Latitude (°N)	Longitude (°E)	Depth (m)	U-Th Age (year)	^{14}C-based calendar age after correction (year)	Final calendar age (year)	Age error (1sd)	δ^{15}N vs AIR (‰)	1sd
DP39	Burdwood Bank	-54.727	-62.248	728	nd	265	265	500	8.44	0.07
DP126	Burdwood Bank	-54.727	-62.223	816	6	277	6	6	7.96	0.21
DP30	Burdwood Bank	-54.727	-62.223	816	nd	446	446	500	8.87	0.07
DP40	Burdwood Bank	-54.727	-62.248	728	nd	457	457	500	8.64	0.18
DP127	Burdwood Bank	-54.727	-62.248	728	nd	1393	1393	500	7.44	0.10
DP41	Burdwood Bank	-54.727	-62.248	728	nd	2329	2329	500	10.32	0.04
DP129	Burdwood Bank	-54.727	-62.248	728	nd	2692	2692	500	9.38	0.35
DP34	Burdwood Bank	-54.727	-62.223	816	nd	2724	2724	500	9.59	0.10
DP42	Burdwood Bank	-54.727	-62.248	728	nd	4004	4004	500	8.70	0.30
XTW-1	Burdwood Bank	-54.727	-62.223	816	nd	4374	4374	500	10.73	0.07
DP124	Burdwood Bank	-54.727	-62.248	728	nd	4484	4484	500	8.78	0.48
XTW-2	Burdwood Bank	-54.727	-62.223	816	nd	5547	5547	500	7.58	0.07
DP125	Burdwood Bank	-54.727	-62.248	728	nd	5818	5818	500	9.55	0.27
DP35	Burdwood Bank	-54.727	-62.223	816	nd	5931	5931	500	10.01	0.10
XTW-3	Burdwood Bank	-54.727	-62.223	816	nd	6076	6076	500	9.62	0.07
XTW-4	Burdwood Bank	-54.727	-62.223	816	nd	6386	6386	500	9.59	0.07
XTW-5	Burdwood Bank	-54.727	-62.248	728	nd	8328	8328	500	10.50	0.07
XTW-6	Burdwood Bank	-54.727	-62.248	728	nd	8524	8524	500	10.09	0.07
DP123	Burdwood Bank	-54.727	-62.248	728	nd	9316	9316	500	11.12	0.19
XTW-7	Burdwood Bank	-54.727	-62.223	816	nd	11372	11372	500	12.54	0.07
DP128	Burdwood Bank	-54.727	-62.223	816	nd	11621	11621	500	11.65	0.15
XTW-8	Burdwood Bank	-54.839	-62.126	1879	nd	14861	14861	500	11.56	0.07
DP29	Burdwood Bank	-54.727	-62.223	816	16343	15045	16343	154	14.08	0.49
XTW-9	Burdwood Bank	-54.839	-62.126	1879	nd	15236	15236	500	11.98	0.07
DP102	Cape Horn	-57.166	-67.103	1012	nd	1191	1191	500	6.84	0.08
DP4	Cape Horn	-57.306	-66.8510	647	nd	1370	1370	500	7.18	0.19
DP122	Cape Horn	-57.361	-66.682	1441	nd	1683	1683	500	8.61	0.10
DP119	Cape Horn	-57.361	-66.682	1441	nd	2049	2049	500	9.41	0.02
DP31	Cape Horn	-57.306	-66.8510	647	nd	2303	2303	500	7.00	0.19
DP3	Cape Horn	-57.306	-66.8510	647	nd	2462	2462	500	8.09	0.16

DP6	Cape Horn	-57.306	-66.8510	647	nd	2534	2534	500	9.23	0.09
DP32	Cape Horn	-57.306	-66.8510	647	nd	2613	2613	500	7.98	0.12
DP120	Cape Horn	-57.361	-66.682	1441	nd	2896	2896	500	8.61	0.15
DP16	Cape Horn	-57.276	-67.2402	1872	nd	3069	3069	500	8.17	0.05
DP118	Cape Horn	-57.361	-66.682	1441	nd	3263	3263	500	9.88	0.07
DP14	Cape Horn	-57.276	-67.2402	1872	nd	3318	3318	500	8.04	0.09
DP5	Cape Horn	-57.306	-66.8510	647	nd	3426	3426	500	8.53	0.30
DP121	Cape Horn	-57.361	-66.682	1441	nd	4336	4336	500	8.88	0.02
DP104	Cape Horn	-57.166	-67.103	1012	nd	4347	4347	500	8.28	0.06
DP106	Cape Horn	-57.166	-67.103	1012	nd	9245	9245	500	9.85	0.09
DP33	Cape Horn	-57.306	-66.8510	647	nd	11056	11056	500	12.02	0.06
DP105	Cape Horn	-57.166	-67.103	1012	nd	11340	11340	500	11.50	0.17
DP103	Cape Horn	-57.166	-67.103	1012	nd	11428	11428	500	11.20	0.38
DP17	Cape Horn	-57.276	-67.2402	1872	nd	15301	15301	500	11.83	0.14
XTW-11	Cape Horn	-57.276	-67.2402	1872	nd	15519	15519	500	11.02	0.07
DP7	Interim Seamount	-60.567	-65.9750	904	nd	9472	9472	500	10.87	0.04
DP62	Interim Seamount	-60.606	-66.004	1064	nd	12740	12740	500	12.03	0.13
DP66	Interim Seamount	-60.601	-66.002	1196	nd	14819	14819	500	12.11	0.02
DP65	Interim Seamount	-60.601	-66.002	1196	15221	15005	15221	72	12.36	0.18
DP110	Interim Seamount	-60.5464	-65.953	1134	21466	21266	21466	109	15.68	0.30
DP114	Interim Seamount	-60.601	-66.002	1196	nd	30828	30828	500	11.92	0.03
DP1	Sars Seamount	-59.7197	-68.869	658	nd	624	624	500	9.05	0.23
XTW-12	Sars Seamount	-59.728	-68.9000	776	nd	802	802	500	8.51	0.07
XTW-13	Sars Seamount	-59.728	-68.9000	776	nd	1314	1314	500	9.68	0.07
XTW-14	Sars Seamount	-59.764	-68.936	981	nd	1333	1333	500	7.92	0.07
XTW-57	Sars Seamount	-59.7298	-68.934	1323	nd	1559	1559	500	8.14	0.07
DP90	Sars Seamount	-59.7201	-68.865	647	nd	1676	1676	500	8.08	0.15
DP91	Sars Seamount	-59.7201	-68.865	647	nd	2056	2056	500	7.97	0.27
DP78	Sars Seamount	-59.797	-68.965	1701	nd	2223	2223	500	10.76	0.16
DP57	Sars Seamount	-59.7197	-68.869	658	nd	3482	3482	500	10.10	0.18
XTW-15	Sars Seamount	-59.728	-68.9000	776	nd	3600	3600	500	8.16	0.07
XTW-16	Sars Seamount	-59.728	-68.9000	776	nd	3767	3767	500	8.94	0.07
DP76	Sars Seamount	-59.797	-68.965	1701	nd	4133	4133	500	10.86	0.01
XTW-17	Sars Seamount	-59.728	-68.9000	776	nd	4183	4183	500	9.45	0.07
XTW-18	Sars Seamount	-59.728	-68.9000	776	nd	4381	4381	500	9.88	0.07
XTW-19	Sars Seamount	-59.728	-68.9000	776	nd	4394	4394	500	7.30	0.07

DP55	Sars Seamount	-59.7197	-68.869	658	nd	4488	4488	500	9.40	0.23
DP89	Sars Seamount	-59.7201	-68.865	647	nd	5029	5029	500	8.76	0.13
DP81	Sars Seamount	-59.797	-68.965	1701	nd	5186	5186	500	10.04	0.08
DP58	Sars Seamount	-59.7197	-68.869	658	nd	5401	5401	500	10.76	0.17
DP59	Sars Seamount	-59.7197	-68.869	658	nd	5651	5651	500	8.82	0.05
XTW-21	Sars Seamount	-59.732	-68.746	869	nd	6599	6599	500	10.05	0.07
DP92	Sars Seamount	-59.7197	-68.869	658	nd	6600	6600	500	10.83	0.12
DP82	Sars Seamount	-59.797	-68.965	1701	nd	6884	6884	500	9.88	0.03
DP54	Sars Seamount	-59.764	-68.936	981	nd	7511	7511	500	8.36	0.29
DP95	Sars Seamount	-59.7520	-68.904	843	nd	7634	7634	500	9.52	0.30
DP86	Sars Seamount	-59.7201	-68.865	647	nd	7765	7765	500	10.55	0.19
DP80	Sars Seamount	-59.797	-68.965	1701	nd	7828	7828	500	10.95	0.11
DP56	Sars Seamount	-59.7197	-68.869	658	nd	8043	8043	500	10.42	0.07
DP97	Sars Seamount	-59.7520	-68.904	843	nd	8097	8097	500	10.06	0.29
DP64	Sars Seamount	-59.72	-68.806	692	nd	8389	8389	500	9.28	0.11
DP83	Sars Seamount	-59.797	-68.965	1701	nd	8798	8798	500	11.56	0.02
DP60	Sars Seamount	-59.764	-68.936	981	nd	9024	9024	500	9.73	0.28
DP73	Sars Seamount	-59.797	-68.965	1701	nd	9541	9541	500	10.61	0.06
DP87	Sars Seamount	-59.7201	-68.865	647	nd	9552	9552	500	9.87	0.44
XTW-22	Sars Seamount	-59.721	-68.883	695	nd	9554	9554	500	9.39	0.07
DP109	Sars Seamount	-59.721	-68.883	695	10196	9631	10196	41	11.13	0.29
XTW-23	Sars Seamount	-59.705	-69.007	1750	nd	10889	10889	500	10.66	0.07
DP72	Sars Seamount	-59.797	-68.965	1701	nd	11080	11080	500	12.20	0.01
DP11	Sars Seamount	-59.7197	-68.869	658	nd	11238	11238	500	8.85	0.34
XTW-24	Sars Seamount	-59.721	-68.883	695	nd	11279	11279	500	10.27	0.07
XTW-25	Sars Seamount	-59.721	-68.883	695	nd	11286	11286	500	9.51	0.07
DP12	Sars Seamount	-59.7197	-68.869	658	nd	11299	11299	500	10.87	0.04
DP108	Sars Seamount	-59.721	-68.883	695	11305	11306	11305	61	9.91	0.18
DP93	Sars Seamount	-59.738	-68.902	957	nd	11364	11364	500	11.04	0.30
XTW-26	Sars Seamount	-59.721	-68.883	695	nd	11366	11366	500	9.01	0.07
DP2	Sars Seamount	-59.741	-68.9	978	11549	11392	11549	65	8.92	0.11
DP116	Sars Seamount	-59.721	-68.883	695	11317	11436	11317	36	8.90	0.16
DP88	Sars Seamount	-59.7201	-68.865	647	nd	11466	11466	500	9.89	0.13
DP9	Sars Seamount	-59.7197	-68.869	658	nd	11481	11481	500	9.96	0.10

XTW-27	Sars Seamount	-59.721	-68.883	695	nd	11518	11518	500	9.99	0.07
XTW-28	Sars Seamount	-59.721	-68.883	695	nd	11579	11579	500	9.34	0.07
DP10	Sars Seamount	-59.7197	-68.869	658	nd	11581	11581	500	9.59	0.05
DP99	Sars Seamount	-59.7520	-68.904	843	nd	11603	11603	500	10.18	0.07
DP79	Sars Seamount	-59.797	-68.965	1701	nd	11663	11663	500	9.96	0.12
DP45	Sars Seamount	-59.764	-68.936	981	nd	11807	11807	500	10.20	0.13
DP67	Sars Seamount	-59.797	-68.965	1701	nd	12078	12078	500	10.90	0.00
DP51	Sars Seamount	-59.764	-68.936	981	nd	12189	12189	500	11.11	0.13
XTW-29	Sars Seamount	-59.705	-69.007	1750	nd	12304	12304	500	9.66	0.07
DP69	Sars Seamount	-59.797	-68.965	1701	nd	12375	12375	500	8.97	0.08
DP84	Sars Seamount	-59.797	-68.965	1701	nd	12533	12533	500	11.45	0.03
DP74	Sars Seamount	-59.797	-68.965	1701	nd	12558	12558	500	9.18	0.36
DP70	Sars Seamount	-59.797	-68.965	1701	nd	12655	12655	500	11.83	0.09
XTW-30	Sars Seamount	-59.705	-69.007	1750	nd	12690	12690	500	10.85	0.07
DP77	Sars Seamount	-59.797	-68.965	1701	nd	12821	12821	500	10.71	0.06
DP75	Sars Seamount	-59.797	-68.965	1701	14051	13829	14051	81	13.00	0.20
DP43	Sars Seamount	-59.764	-68.936	981	nd	13959	13959	500	11.06	0.08
XTW-31	Sars Seamount	-59.764	-68.936	981	nd	13994	13994	500	11.36	0.07
DP107	Sars Seamount	-59.721	-68.883	695	nd	14043	14043	500	9.65	0.28
XTW-33	Sars Seamount	-59.764	-68.936	981	nd	14261	14261	500	10.28	0.07
XTW-34	Sars Seamount	-59.764	-68.936	981	nd	14334	14334	500	11.15	0.07
XTW-35	Sars Seamount	-59.764	-68.936	981	nd	14389	14389	500	11.62	0.07
XTW-36	Sars Seamount	-59.764	-68.936	981	nd	14528	14528	500	10.21	0.07
XTW-37	Sars Seamount	-59.764	-68.936	981	nd	14560	14560	500	12.04	0.07
DP85	Sars Seamount	-59.797	-68.965	1701	nd	14562	14562	500	14.00	0.01
XTW-38	Sars Seamount	-59.764	-68.936	981	nd	14588	14588	500	10.09	0.07
XTW-39	Sars Seamount	-59.764	-68.936	981	nd	14603	14603	500	11.70	0.07
DP46	Sars Seamount	-59.764	-68.936	981	nd	14645	14645	500	12.49	0.16
XTW-40	Sars Seamount	-59.764	-68.936	981	nd	14645	14645	500	11.40	0.07
DP96	Sars Seamount	-59.7520	-68.904	843	nd	14785	14785	500	10.27	0.11
XTW-41	Sars Seamount	-59.764	-68.936	981	nd	14832	14832	500	10.18	0.07
DP37	Sars Seamount	-59.797	-68.965	1701	nd	14846	14846	500	12.51	0.09
XTW-42	Sars Seamount	-59.764	-68.936	981	nd	14873	14873	500	11.41	0.07
XTW-43	Sars Seamount	-59.764	-68.936	981	nd	14882	14882	500	11.88	0.07

XTW-44	Sars Seamount	-59.764	-68.936	981	nd	14884	14884	500	11.18	0.07
DP61	Sars Seamount	-59.764	-68.936	981	nd	14952	14952	500	12.88	0.04
XTW-45	Sars Seamount	-59.764	-68.936	981	nd	15025	15025	500	11.66	0.07
XTW-46	Sars Seamount	-59.764	-68.936	981	nd	15043	15043	500	12.15	0.07
DP36	Sars Seamount	-59.797	-68.965	1701	nd	15049	15049	500	13.63	0.01
XTW-47	Sars Seamount	-59.764	-68.936	981	nd	15074	15074	500	11.76	0.07
XTW-48	Sars Seamount	-59.764	-68.936	981	nd	15086	15086	500	11.87	0.07
XTW-49	Sars Seamount	-59.7520	-68.904	843	nd	15108	15108	500	11.92	0.07
DP71	Sars Seamount	-59.797	-68.965	1701	nd	15137	15137	500	12.30	0.08
XTW-50	Sars Seamount	-59.764	-68.936	981	nd	15225	15225	500	11.20	0.07
DP68	Sars Seamount	-59.797	-68.965	1701	nd	15251	15251	500	13.86	0.07
XTW-51	Sars Seamount	-59.764	-68.936	981	nd	15336	15336	500	11.14	0.07
XTW-52	Sars Seamount	-59.764	-68.936	981	nd	15426	15426	500	11.98	0.07
DP48	Sars Seamount	-59.764	-68.936	981	16851	17442	16851	168	12.61	0.27
DP94	Sars Seamount	-59.7520	-68.904	843	nd	28523	28523	500	12.47	0.06
DP53	Sars Seamount	-59.764	-68.936	981	nd	30054	30054	500	11.29	0.06
DP44	Sars Seamount	-59.764	-68.936	981	nd	39000	39000	500	12.95	0.19
DP18	Shackleton Fracture Zone	-60.179	-57.837	806	nd	7390	7390	500	11.02	0.23
DP27	Shackleton Fracture Zone	-60.1790	-57.836	823	nd	13128	13128	500	12.81	0.10
DP19	Shackleton Fracture Zone	-60.179	-57.837	806	18047	18235	18047	168	12.51	0.08
XTW-53	Shackleton Fracture Zone	-60.1790	-57.836	823	nd	18978	18978	500	12.35	0.07
XTW-54	Shackleton Fracture Zone	-60.1790	-57.836	823	nd	19982	19982	500	13.38	0.07
XTW-55	Shackleton Fracture Zone	-60.1790	-57.836	823	nd	20134	20134	500	13.86	0.07
DP13	Shackleton Fracture Zone	-60.1790	-57.836	823	20367	20840	20367	58	12.98	0.05
DP22	Shackleton Fracture Zone	-60.1790	-57.836	823	nd	21572	21572	500	11.74	0.06
DP21	Shackleton Fracture Zone	-60.179	-57.837	806	22578	22602	22578	81	13.70	0.05
DP23	Shackleton Fracture Zone	-60.1790	-57.836	823	nd	23141	23141	500	12.23	0.06
DP25	Shackleton Fracture Zone	-60.1790	-57.836	823	nd	24045	24045	500	12.68	0.04

XTW-56	Shackleton Fracture Zone	-60.182	-57.828	819	nd	25630	25630	500	13.01	0.07
DP28	Shackleton Fracture Zone	-60.1790	-57.836	823	27159	26357	27159	122	12.48	0.05
DP26	Shackleton Fracture Zone	-60.1790	-57.836	823	nd	28144	28144	500	12.23	0.04
DP24	Shackleton Fracture Zone	-60.1790	-57.836	823	nd	31281	31281	500	11.99	0.13
XTW-58	Shackleton Fracture Zone	-60.182	-57.828	819	nd	35682	35682	500	12.19	0.07
DP20	Shackleton Fracture Zone	-60.179	-57.837	806	nd	36754	36754	500	12.86	0.27